ABSTRACT

Title of Document:	LONGITUDINAL SPACE-CHARGE WAVES INDUCED BY ENERGY MODULATIONS
	Brian L. Beaudoin, Master of Science, 2008
Directed By:	Professor Patrick G. O'Shea and Professor Rami A. Kishek Department of Electrical and Computer Engineering

High intensity beams that are space-charge dominated are important for applications such as free electron lasers that require high intensity and low emittance beams. Modulations in energy or density can induce space-charge waves at low energies which could be problematic at higher energies. This thesis is a study of longitudinal space-charge waves induced by energy modulations within a highly space-charge dominated beam propagating in the University of Maryland Electron Ring (UMER). Using an induction cell, we present the first UMER experimental results on the design and application of the cell to place energy perturbations. We compare the results to one-dimensional cold fluid theory and simulation. We allow the perturbation to propagate for over 60 m so that we can get a turn by turn measurement of the experimental sound speed. In some of the turn by turn data, we obtain a 4.8% disagreement between the experimentally measured sound speed and theory.

LONGITUDINAL SPACE-CHARGE WAVES INDUCED BY ENERGY
MODULATIONS

By

Brian L. Beaudoin

Thesis submitted to the Faculty of the Graduate School of the
University of Maryland, College Park, in partial fulfillment
of the requirements for the degree of
Master of Science
2008

Advisory Committee:
Professor Patrick G. O'Shea, Chair
Professor Rami A. Kishek
Professor Victor L. Granatstein

Dedication

to my best friend and life partner,

Jennifer

Acknowledgements

First, I would like to thank both of my advisors, Professor Patrick G. O'Shea and Professor Rami A. Kishek for guiding me through the successful completion of my thesis. I would like to also thank them for providing their encouragement and advice and most important, enthusiasm throughout this process. I would like to also thank Professor Martin Reiser for his support.

I would like to thank Dr. Santiago Bernal for his invaluable help and the atmosphere he brings with him. I would like to thank Dr. Irving Haber and Dr. David Sutter for being there to continually challenge me. I am grateful to the students of UMER, Charles Tobin, Christos Papadopoulos, Chao Wu, Dr. Kai Tian, Dr. Diktys Stratakis, Jeffrey Birenbaum, David Park, Matthew Bakalar, for both their assistance and guidance with this work. I would also like to thank former members of UMER, Dr. Mark Walter and Bryan Quinn.

I would like to also thank Professor Victor L. Granatstein for serving on my thesis examination committee.

Finally, I would like to thank the support of the United States Department of Energy Offices, of High Energy Physics and High Energy Density Physics, and by the United States Department of Defense, Office of Naval Research and Joint Technology Office

Table of Contents

List of Tables

List of Figures

Chapter 1: Introduction

Intense particle beams are of interest in many applications requiring high quality beams transported over extended distances; such as spallation neutron sources [1], accelerator driven High Energy Density Physics (HEDP) [2], and Free Electron Lasers (FELs) [3]. In all cases, beams at the source are born as space-charge dominated and the performance depends on the quality of the beam at the end of the accelerator both transversely and longitudinally. The beam quality can be negatively impacted by nonlinear space-charge forces which can result from fluctuations in beam density or energy, and can lead to instabilities.

A detailed understanding of how the collective space-charge effects in a space-charge dominated beam can reduce the quality of a beam is key to a successful operating machine. This thesis explores how one of these space-charge effects, i.e., longitudinal space-charge waves, could be launched with the application of longitudinal electric fields. These fields create a velocity modulation within the beam that launches a pair of waves traveling along the beam ultimately creating a density modulation [4].

In section 1.1, we describe the motivation for this work. In section 1.2, the background and general history of longitudinal space-charge waves is described and finally in section 1.3, we describe the organization of the thesis.

1.1 Motivation

The understanding of longitudinal space-charge waves is important at both low-energies as well as high-energies. Beams at the source are likely in the space charge dominated regime. Any perturbations in either density or velocity space will induce space-charge waves in this regime. Since the wave phase velocity or sound speed of these space-charge waves scales as the inverse of gamma to the 5/2 power [5], the perturbations will travel along the beam, but if the beam is to be accelerated to higher energies these modulations will slow down and eventually become frozen into the beam.

As will be explained in section 2.1, each of these waves carries a velocity component that is equal to the beam velocity plus the sound speed for the fast wave and the beam velocity minus the sound speed for the slow wave. The off-energy particles within the waves interact with a dispersive lattice such as a storage ring, which then has the potential to cause problems. Within the magnetic bending sections of a ring, the energy modulations can excite Coherent Synchrotron Radiation (CSR), which will lead to emittance growth [6], beam instability and micro-bunching [7]. This emittance growth would also lead to a decrease in the brightness of the beam since it is inversely proportional to the square of the emittance [5].

With Free Electron Lasers (FELs), emittance growth could also lead to an increase in the gain length required to obtain full power in the undulator and also decrease the emitted power [3]. Therefore, it is important for machines that contain intense beams, to properly study and understand longitudinal space-charge waves, how they evolve and propagate on the beam.

1.2   Background and history

A charged particle beam is a group of particles moving closely along a reference trajectory defined by the bending elements. Externally applied focusing forces from focusing elements such as solenoidal or quadrupole lens balance the space-charge fields or self-fields of the beam which acts to defocus the beam transversely. The self-fields consist of an electric field due to the coulomb repulsion between electrons, and a magnetic field due to the motion of the charged particles.

The thermal pressure or emittance of the beam can be attributed to various reasons, such as; mismatches between the beam envelope and focusing elements, injection errors, can all act to defocus the beam by heating it up. Transverse emittance is a measure of the beam quality or the thermal pressure inside the beam, which is the product of the beam's width and the random (or thermal) velocity spread [5].

In the longitudinal direction, there is also an emittance term and space-charge fields present which defocus the beam longitudinally. In order to contain the beam in the longitudinal direction, a longitudinal focusing electric field could be used to compensate for these forces, or, if there is an appropriate energy versus time slew in the beam, a magnetic bunch compressor (a series of dipole magnets in a chicane) could be used to compress the beam longitudinally. The types of longitudinal focusing fields applied are dependent on the charge distribution of the bunch; i.e. compressing a space charge dominated beam with a parabolic line charge profile would require different fields then that for a rectangular profile. If the focusing bucket

does not match the beam profile or if there are errors in the focusing fields themselves, this longitudinal mismatch will launch space-charge waves on the beam.

The history of space-charge waves goes back to Simon Ramo and W.C. Hahn with their investigations of space-charge waves in vacuum tubes [8, 9]. In the 1950s, Birdsall and Whinnery performed calculations of gain and phase of electrons passing near lossy walls which was used for beam amplification [10].

The classical method for modeling space-charge waves uses a one-dimensional cold fluid model [5]. This model treats the particles in the beam as a continuous medium and assumes zero temperature to truncate the fluid equation hierarchy, resulting in the momentum and continuity equations. By adding a small perturbation and linearizing those equations, one obtains a description for the forward and backward going waves [5].

At the University of Maryland Charged Particle Beam Laboratory, the ability to generate controlled perturbations was pioneered through experimental investigations of space-charge waves by J.G. Wang and D.X. Wang [11]. They observed the evolution of space-charge waves created from electrical perturbations at the gun and also the evolution of a single wave where either the slow wave or the fast wave was selected based on the initial conditions at the gun. This work was further advanced by Hyyong Suk to understand the resistive wall instability [12]. A resistive wall adds feedback leading to the decay in amplitude of the fast wave and a growth in amplitude of the slow wave. Yun Zou increased the amplitudes of the perturbations, so to bring the waves into the non-linear regime where the waves would no longer travel in a non-dispersive manner [13]. Yupeng Cui developed the high resolution

energy analyzer and Kai Tian measured the velocity profiles of the density initiated perturbations with the analyzer, confirming the 1-D cold fluid model [4, 13].

With the advent of the University of Maryland Electron Ring (UMER), new methods have been developed to generate controlled perturbations. Yijie Huo began the work of using an ultraviolet laser focused onto the dispenser cathode of the UMER gun, extracting current from the cathode through photoemission [14]. John Harris extended this work to more then half the ring and Jayakar C.T. Thangaraj continued this work with the multi-turn transport of this laser induced electron beam [15]. He also observed an instability when over driving the cathode with the laser, which leads to virtual cathode oscillations [16, 17].

This thesis is a study of longitudinal space-charge waves induced by energy modulations using a new technique that utilizes an induction cell. The first UMER experimental results are compared to one-dimensional cold fluid theory and simulation. Allowing the perturbation to propagate for over 60 m, we obtain a turn by turn measurement of the experimental sound speed. In some of the turn by turn data, we obtain a 4.8% disagreement between the experimentally measured sound speed and theory.

1.3   Organization of thesis

In chapter 2, we review the 1-D cold fluid model and dispersion relation for longitudinal space-charge waves from which we define the wave speed and g-factor. We also compare the characteristics of the waves generated by pure initial density perturbations versus pure initial velocity perturbations.

In chapter 3, we designed, model, simulate and describe the experimental setup for the induction cell, which we operate both as a way to perturb the beam velocity and for longitudinal focusing. This cell can also be operated as a wall current monitor if the frequency response of the device is readjusted. We go through some of the basic limitations of the cell and calculate and compare the focal length of the cell to that of quadrupoles within UMER.

In chapter 4, we present the first UMER experimental results on the application of the induction cell to place energy perturbations on the flat region of the beam. Both positive and negative perturbations are investigated, comparing the experimental results to 1-D cold fluid simulations. We then allow the beam to propagate for over 60 m so that the space-charge waves have sufficient time to split and experimental sound speeds are extracted on a turn by turn basis.

Finally, chapter 5 summarizes the new results and explores other topics for future research.

Chapter 2: Theory of Space-Charge Waves

In this chapter we review the theory of longitudinal wave propagation in a beam that is highly space charge dominated. The purpose of this chapter is to analyze what happens to the wave polarities and their corresponding amplitudes when an initial perturbation is either a pure density modulation or a pure velocity modulation. In section 2.1, the one-dimensional cold fluid model is presented along with the sound speed C_s, and the dispersion relation for an infinitely long cylindrical beam inside a conductive pipe. In section 2.2, the evolution of the velocity and density initiated perturbations are analyzed in terms of their polarities and amplitudes for both the fast and slow waves launched on the beam.

2.1 Analysis of space-charge waves using the one dimensional fluid model

The cold fluid model represents the beam as a continuous 1-D fluid and assumes zero temperature so as to truncate the fluid equation hierarchy. This corresponds to a laminar beam where all the electrons are moving in parallel layers. It is also assumed that the beam is an infinitely long cylinder of charge with an average radius equal to $\bar{R}$, inside a drift tube of radius b where the line-charge density is given by λ. The beams velocity is given by v and so the product λv is equal to the beam current I.

For small perturbations we can linearize the momentum and continuity equations by writing the line charge density, velocity and beam current as the sum of constant plus perturbed quantities [5].

$$\lambda(z,t) = \lambda_0 + \lambda_1 e^{i(\omega t - kz)}$$
$$v(z,t) = v_0 + v_1 e^{i(\omega t - kz)} \tag{2.1}$$
$$I(z,t) = I_0 + I_1 e^{i(\omega t - kz)}$$

The quantities with the subscript 0 represent the constant or "DC" part of the beam and the subscript 1 represents the time and space varying perturbations. After linearizing the continuity and momentum equations and performing the necessary Fourier transforms, we obtain the dispersion relation as well as the sound speed of the beam [5].

$$(\omega - v_0 k)^2 = \frac{q}{\gamma_0^3 m} \frac{g}{4\pi\varepsilon_0 \gamma_0^2} \lambda_0 k^2 = C_s^2 k^2 \tag{2.2}$$

$$C_s = \sqrt{\frac{q}{\gamma_0^3 m} \frac{g}{4\pi\varepsilon_0 \gamma_0^2} \lambda_0} \tag{2.3}$$

Where q is the electron charge, m the electron mass, γ_0 the Lorentz factor, ε_0 the relative permittivity and the variable g is a geometry factor that accounts for the transverse forces [5].

$$g = 2\ln\left(\frac{b}{\overline{R}}\right) \tag{2.4}$$

Here we assume a long beam so that the radius doesn't change and zero pressure, so that the beam is fully space-charge dominated. The phase velocities of the two space-charge waves are equal to the beam velocity plus the sound speed for the fast wave and the beam velocity minus the sound speed for the slow wave.

$$v_f = v_0 + C_s$$
$$v_s = v_0 - C_s$$

(2.5)

The quantities v_f and v_s are the fast wave and slow wave velocities respectively.

Since the phase velocities are independent of frequency, the space-charge waves are

non-dispersive and so the shape of the wave will not be distorted as it propagates

along the beam.

2.2 Velocity versus density perturbations

The analytical solution for the propagation of space-charge waves uses the

linearized continuity and momentum equations, which are then Laplace transformed

in both time and space. Solving the algebraic equations and applying inverse

transformations, the perturbed line-charge density, velocity and current are obtained,

where the sign on top of the $p\left(t - \dfrac{z}{v_0 \mp C_s}\right)$ smooth varying function of magnitude

equal to unity is for the slow wave and the sign on the bottom is for the fast wave

[11]. We also assume the initial density or velocity perturbation is launched at $t = 0^+$

where we use $\delta = \dfrac{v_1\left(0, t = 0^+\right)}{v_0}$ to denote the magnitude of the velocity perturbation at

$t = 0^+, z = 0$ and $\eta = \dfrac{I_1\left(0, t = 0^+\right)}{I_0}$ to denote the magnitude of the current perturbation

at $t = 0^+, z = 0$.

$$\lambda_1(z,t) = \mp \frac{\lambda_0}{2}\left[\delta\frac{v_0}{C_s} \mp (\eta - \delta)\right]p\left(t - \frac{z}{v_0 \mp C_s}\right)$$

(2.6 a)

9

$$v_1(z,t) = \frac{v_0}{2}\left[\delta \mp (\eta - \delta)\frac{C_s}{v_0}\right]p\left(t - \frac{z}{v_0 \mp C_s}\right) \qquad (2.6\text{ b})$$

$$I_1(z,t) = \mp \frac{I_0}{2}\left[\delta \frac{v_0}{C_s} \mp \eta + (\eta - \delta)\frac{C_s}{v_0}\right]p\left(t - \frac{z}{v_0 \mp C_s}\right) \qquad (2.6\text{ c})$$

We can rewrite equations 2.6a, b and c by converting the equations into the beam

frame by using $z^* = z - v_0 t$.

$$\lambda_1(z,t) = \mp \frac{\lambda_0}{2}\left[\delta \frac{v_0}{C_s} \mp (\eta - \delta)\right]p\left(t \pm \frac{z^*}{C_s}\right) \qquad (2.7\text{ a})$$

$$v_1(z,t) = \frac{v_0}{2}\left[\delta \mp (\eta - \delta)\frac{C_s}{v_0}\right]p\left(t \pm \frac{z^*}{C_s}\right) \qquad (2.7\text{ b})$$

$$I_1(z,t) = \mp \frac{I_0}{2}\left[\delta \frac{v_0}{C_s} \mp \eta + (\eta - \delta)\frac{C_s}{v_0}\right]p\left(t \pm \frac{z^*}{C_s}\right) \qquad (2.7\text{ c})$$

The signs in the unity function $p(t)$ are flipped so that the fast wave is the sign on

the bottom and the sign on top is the slow wave.

Space-charge waves can be launched from either an initial density

perturbation or an initial velocity perturbation. If an initially pure density perturbation

was placed onto the beam then δ must be set to zero. With that condition we obtain

from eqn 2.7a, b and c,

$$\lambda_1(z,t) = \frac{\lambda_0}{2}[\eta]p\left(t \pm \frac{z^*}{C_s}\right) \qquad (2.8\text{ a})$$

$$v_1(z,t) = \mp \frac{C_s}{2}[\eta]p\left(t \pm \frac{z^*}{C_s}\right) \qquad (2.8\text{ b})$$

$$I_1(z,t) = \mp \frac{I_0}{2}\left[\eta\left(\frac{C_s}{v_0} \mp 1\right)\right]p\left(t \pm \frac{z^*}{C_s}\right) \qquad (2.8\text{ c})$$

The amplitudes of the line-charge density function for both the fast and slow waves in equation 2.8a has the same polarity as the perturbation, whereas the velocity space function, eqn. 2.8b, the amplitude of the slow wave has the opposite polarity. The last equation, 2.8c, can be approximated by assuming $\frac{C_s}{v_0} \ll 1$ so it can be rewritten as eqn. 2.9.

$$I_1(z,t) = \frac{I_0}{2}[\eta] p\left(t \pm \frac{z^*}{C_s}\right) \tag{2.9}$$

So similar to the case of the line-charge density, the current function also has the same polarity for both the fast and slow wave as the initial perturbation.

If an initially pure velocity perturbation was placed onto the beam then η must be set to zero.

$$\lambda_1(z,t) = \mp \frac{\lambda_0}{2}\left[\delta\left(\frac{v_0}{C_s} \pm 1\right)\right] p\left(t \pm \frac{z^*}{C_s}\right) \tag{2.10 a}$$

$$v_1(z,t) = \frac{v_0}{2}\left[\delta\left(1 \pm \frac{C_s}{v_0}\right)\right] p\left(t \pm \frac{z^*}{C_s}\right) \tag{2.10 b}$$

$$I_1(z,t) = \mp \frac{I_0}{2}\left[\delta\left(\frac{v_0}{C_s} - \frac{C_s}{v_0}\right)\right] p\left(t \pm \frac{z^*}{C_s}\right) \tag{2.10 c}$$

If we once again make the approximation that $\frac{C_s}{v_0} \ll 1$ or $\frac{v_0}{C_s} \gg 1$, then equations 2.10 can be simplified even further.

$$\lambda_1(z,t) = \mp \frac{\lambda_0}{2}\left[\delta\frac{v_0}{C_s}\right] p\left(t \pm \frac{z^*}{C_s}\right) \tag{2.11 a}$$

11

$$v_1(z,t) = \frac{v_0}{2}[\delta] p\left(t \pm \frac{z^*}{C_s}\right) \qquad (2.11 \text{ b})$$

$$I_1(z,t) = \mp \frac{I_0}{2}\left[\delta \frac{v_0}{C_s}\right] p\left(t \pm \frac{z^*}{C_s}\right) \qquad (2.11 \text{ c})$$

In this case we have the opposite scenario. The amplitudes of the velocity function, eqn. 2.11b, have the same polarities for both the fast and slow wave functions as the initial perturbation, whereas in line-charge density space, eqn. 2.11a, the slow wave has the opposite polarity.

The difference between an initial pure density perturbation or an initial pure velocity perturbation is the polarities of both waves in either velocity or line-charge density space.

Chapter 3: Design of the Induction Cell

In Chapter 1 we discussed the need for longitudinal electric fields. For that purpose we use an induction cell to place either accelerating or decelerating fields in the longitudinal direction of varying pulse amplitudes. In this chapter, we discuss the construction and operation of the induction cell and its counterpart, the wall current monitor. In section 3.1 we examine the circuit model of a passive parallel RLC circuit used to measure the beam current. In section 3.2 we add the high-voltage modulator to the circuit and use it to apply longitudinal electric fields to the beam. In section 3.3 we examine the ferrite limitations, both in terms of the induction cell and the wall monitor. In section 3.4 we discuss the electrostatic approximation of the induction cell and calculate the radial field component and finish with the beam optics transfer matrix and a comparison to the quadrupoles in UMER.

3.1   Wall Current Monitor

In this section, we discuss how to use a parallel RLC circuit to measure the image current traveling on the beam pipe.

In UMER, there are three breaks in the beam pipe with a glass insulator installed between the sections of pipe for the vacuum inside the system. These glass gaps create the discontinuity in the conduction path for the image current or return current traveling along the beam pipe. The return current path is completed because of ground loops within the supporting structure of UMER.

Fig 3.1. Glass gap (cross-sectional view)
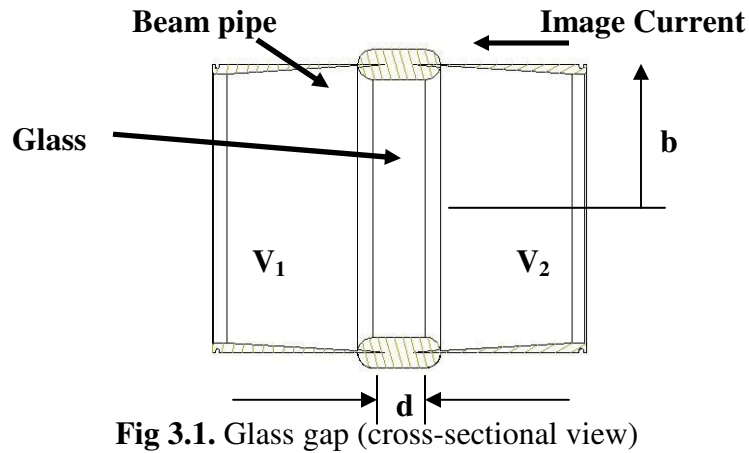
The radius R of the beam pipe is 2.54 cm and the gap separation, d, is 5.08 mm. The beam pipe is mounted to a support plate called a cluster plate with brackets that support the pipe. The electrical contact is made by the bracket and the pipe on either side of the glass gap.

Fig 3.2. Cluster plate assembly
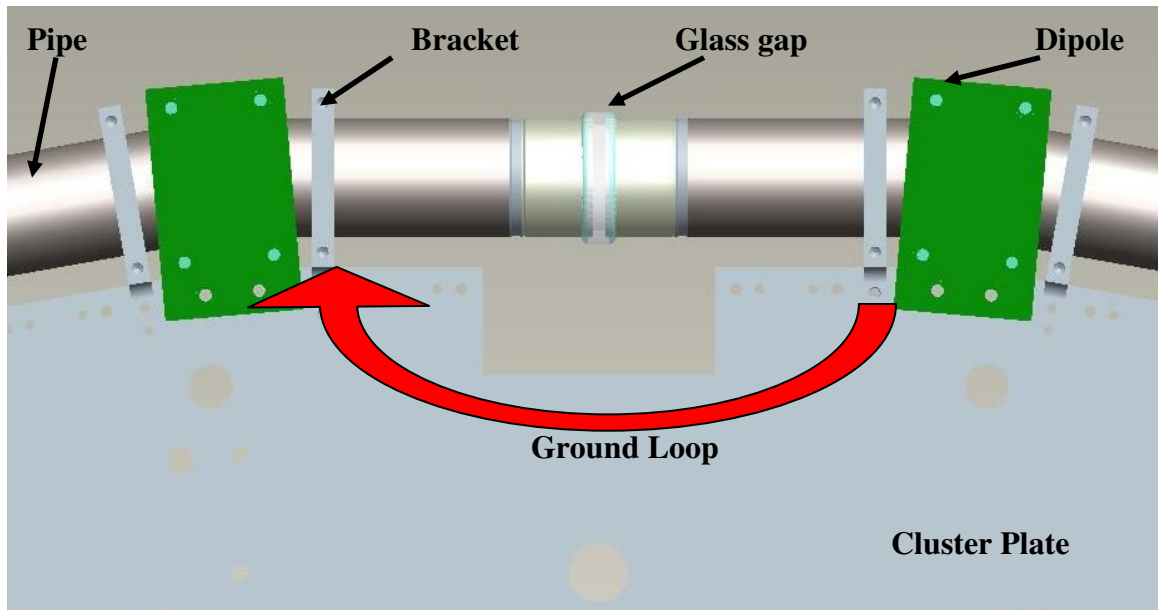
The inductance term or the L of the circuit comes from the ground loop which was calculated to be 7.5 nH. Inductance calculations will be reviewed in section 3.3. Because the resistance of the glass gap is very large, the L/R time constant for this

14

circuit is extremely small. This leads to an induced voltage drop across the gap only during the rising/falling edges of a square beam current pulse. A short time constant for a high-pass filter means that the 3 dB point of the filter is large in frequency space.

In-order to lower the frequency of the pole so that we can measure the entire 100 nsec beam current pulse with minimal droop, we need to extend the time constant of the circuit by adding a resistor across the gap to lower the R and load a ferrite torrid on one side of the gap to increase the inductance of the circuit. An acceptable L/R time constant for this 100 nsec beam with a 2% droop would be 4.95 μsec using $1 - e^{\left(\frac{-t}{\left(\frac{L}{R}\right)}\right)}$.
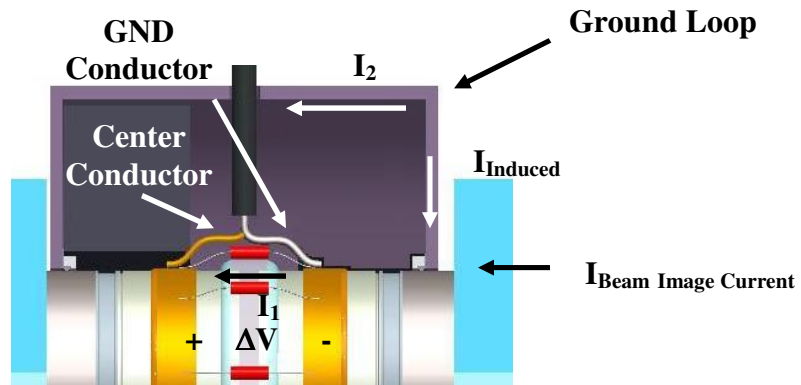
Fig 3.3. Wall current monitor

Before we can measure a voltage using an oscilloscope, we need to understand the current paths and directions so that we can get the polarity of the voltage correct and prevent any accidental short of the measurement with the oscilloscope. As the beam current propagates within UMER, the image current will be propagating in the opposite direction. Since the image current loops the ferrite toroid through the ground loop, this will induce a magnetic flux inside the material.

15

Because of Lenz's law, an equal and opposite current will be generated to oppose the change in flux, we will call that $I_{Induced} = -I_2$. There will also be a current flowing through the resistor across the gap called I_1. The beam image current can be calculated from eqn. 3.1,

$$I_{BeamImageCurrent} = I_1 + I_2 = \frac{\Delta V}{R} + \frac{1}{L}\int \Delta V dt \qquad (3.1)$$

where the ΔV is a measured voltage across the circuit.

There is also a capacitance term associated with the equivalent RLC circuit due the separation of the beam pipe within the glass gap section that has been neglected. If the capacitance is small enough so that the low-pass pole it creates is much higher then the fastest rise time of the square beam current pulse, then the capacitance term can be neglected. Using an LC meter, the measured capacitance of the gap is 22 pF. So if we use a 2 Ω resistor across the gap, the RC time constant would be 0.044 nsec which corresponds to a frequency of 3.61 GHz. The high-frequency pole of this circuit is above the ~1 GHz rise time of the injected square beam pulse so the circuit will not lose any information in the beam up to the 3 dB point. If we use a ferrite toroid with a measured inductance of 9.81 μH, then the low-frequency pole of the circuit will have a 4.9 μsec time constant which would correspond to a 2% droop. The ferrite properties relevant to its choice for UMER along with a calculation of the inductance will be discussed in section 3.3.
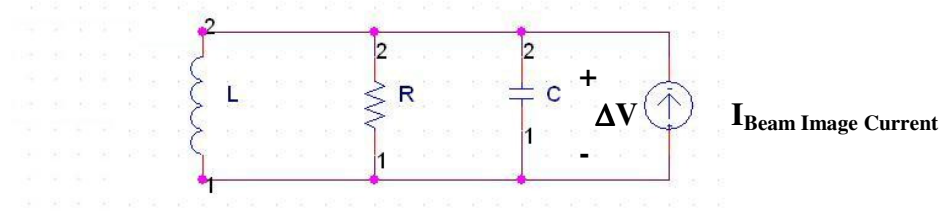
Fig 3.4. Equivalent RLC circuit with the beam image current source

$$\frac{V(s)}{I_{BeamImageCurrent}(s)} = \frac{sLR}{s^2 LRC + sL + R}$$ (3.2)

In this equivalent circuit model, the beam image current is treated as an ideal current source with infinite impedance. The circuit contains two poles, a high-pass pole with a 3 dB point at s = L/R and a low-pass pole with a 3 dB point at s=1/RC. The net circuit forms a band-pass filter and has a frequency response.
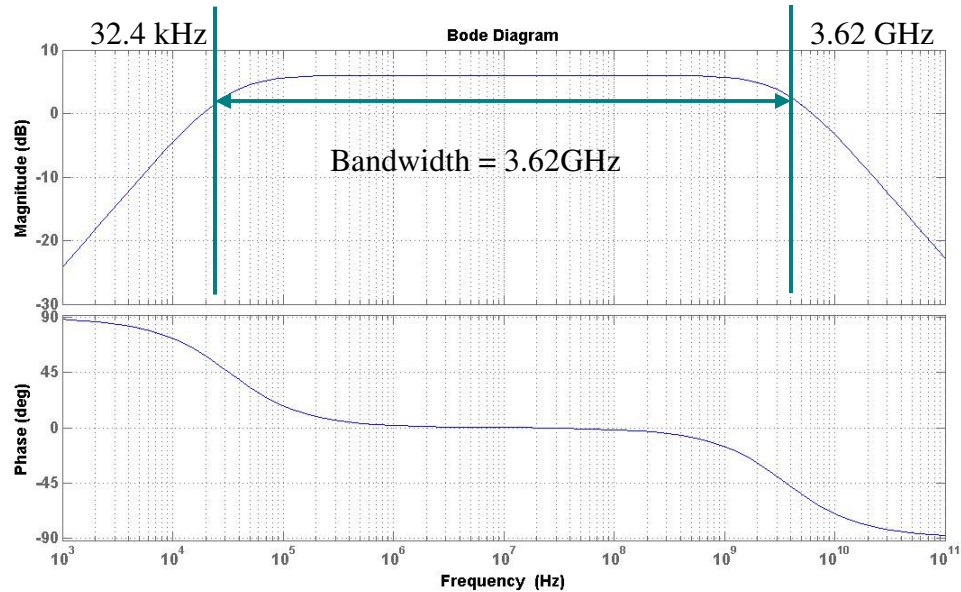
Fig 3.5. Bode plot of circuit model (R = 2 Ω, L = 9.81 μH, C = 22 pF)

Another way of reading the bode diagram is to view the beam image current as composed of multiple frequencies. If any of the frequencies are within the pass-

band of the circuit, then the impedance seen by the current will be 2 Ω. If any of those frequencies are outside of the pass-band, they will be attenuated.

3.2   Induction System

In this section, we will discuss how to use the parallel RLC circuit to apply a potential difference across the gap and apply energy (velocity) perturbations. In section 3.2.1 we will examine the simple high-voltage modulator model that will be used to drive these perturbation fields and compare the results to a bench test of the real circuit. In section 3.2.2 we will examine the circuit model for a coaxial transmission line connecting the modulator and induction cell. In section 3.2.3, modify the parallel RLC circuit to be an induction cell and finally in section 3.2.4, simulate the entire circuit and compare it with test results of the real circuit.

3.2.1   Simple High-Voltage Modulator Model

Since we need to apply kilo-volt delta functions (ear-fields) with a very short pulse width into a low impedance load, a prepackaged switch made by BEHLKE was the best candidate for the application. The specifications for the HTS 80-12-UF are displayed in table 3.1.

Table 3.1. Specifications of HTS 80-12-UF [18]

Parameter	Value
V_{MAX}	8000 volts
I_{PEAK}	120 amps
Pulse Width	10 nsec
Closed-state Resistance	4.5-11.3 Ω
t_{ON} Delay	60 nsec
t_{ON} Rise-time	2.0 nsec

The high-voltage modulator is composed of two of these HTS switches

connected in a bipolar arrangement to provide a positive ear-field and a negative ear-

field. Since the circuit internals are not provided by the manufacturer, a simple switch

model that takes into account the specifications of the HTS units was developed in-

order to simulate the circuit in PSpice.
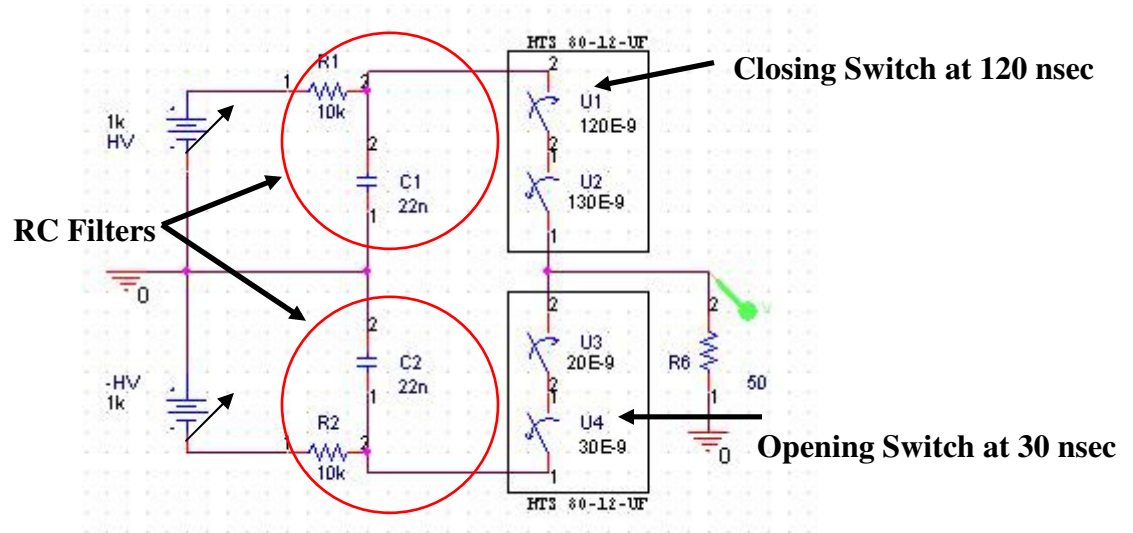
Fig 3.6. Simple high-voltage modulator circuit model

Each of the HTS 80-12-UF units were modeled with an ideal on-switch and an

ideal off-switch in series. The rise/fall times of each of the switches was set to 2.0

nsec as the HTS 80-12-UF units. The closed-state resistance of all the ideal switches

was set to 2.25 Ω so that each pair would be equal to 4.5 Ω. The open-state resistance

was arbitrarily set to 1 Meg since it was not specified in the BEHLKE document. The

period of time that both ideal on and off switches are "on," was initially equal to the

pulse width specifications, i.e. 10 nsec.

The RC filters shown in the circuit are used as a storage element for charge

that is independent of the capacitors internal to the variable power supplies. The

charging time for either of them is 0.22 msec so if the system is pulsed at 60 Hz, the filters have plenty of time to charge. The peak current that either filter can support is 2.2 kA for a 10 nsec pulse using $I = \dfrac{\Delta Q}{\Delta t} = \dfrac{CV}{\Delta t}$ with $V = 1kV$.

A PSpice simulation was performed on the circuit model with the voltage plotted across the 50 Ω resistor versus time.
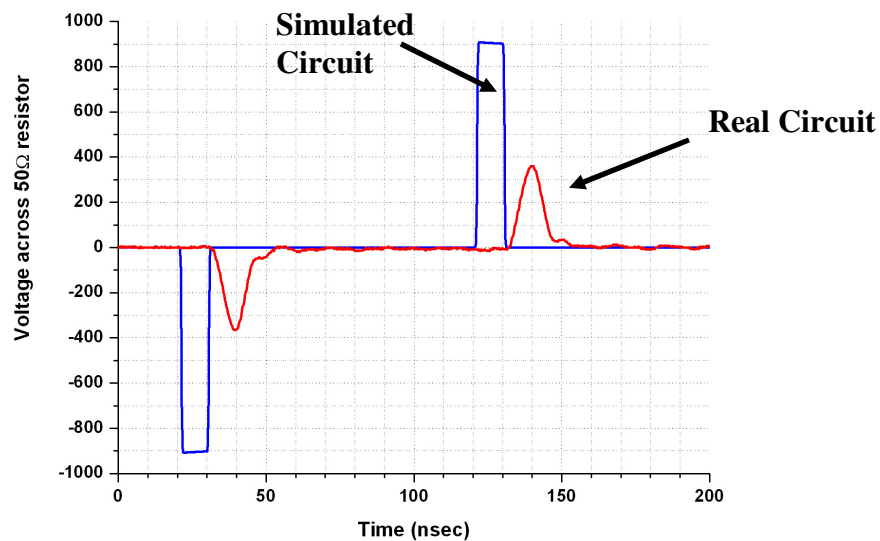
Fig 3.7. Simulated (blue) and real (red) voltage output from modulator across a 50 Ω resistor

In the figure, the voltage output measured from bench test results of the real circuit is not well modeled by the simulation based on the specifications from the manufacture. Both the amplitude of the pulses and the rise times of the simulated pulses are inaccurate. The data from the actual circuit was taken with a 1 GHz oscilloscope and a 1 GHz 100x probe, so the measurement apparatus should not be the cause of the discrepancy. There may be parasitic capacitances affecting the pulse from the switches or there may be a problem with the specifications of these switches.

20

In either case, in order for the PSpice model to better simulate the real modulator circuit, the rise times of each of the ideal switches were modified as well as the period of time that both switches are closed was modified. All the rise/fall times of the ideal switches were changed from 2 nsec to 40 nsec and the period of time that both switches are "closed" was changed from 10 to 15.3 nsec and the circuit was simulated again.
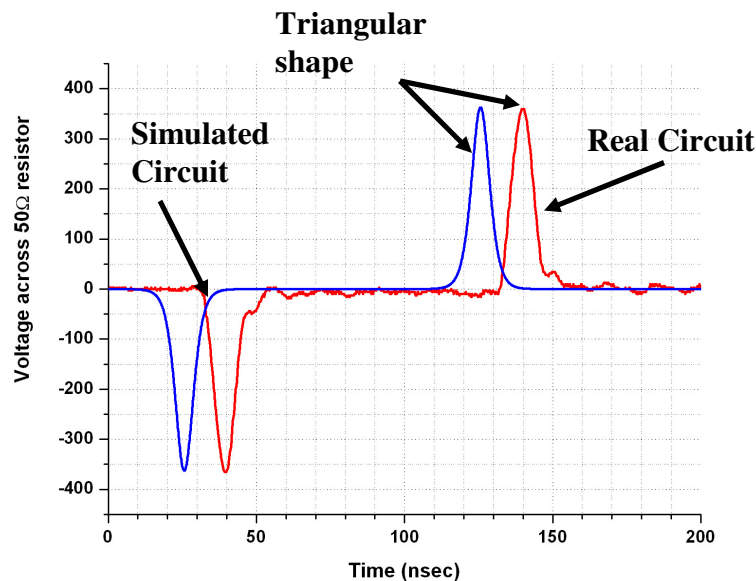
Fig 3.8. Modification of simulation to better represent real circuit

These particular pulse specifications forms triangular shaped pulses that represent the real circuit output. The FWHM of the actual circuit is 8.8 nsec and the FWHM of the simulated circuit is 7.39 nsec. The real circuit is slightly wider in width. The pulse does not reach the full potential provided by the resistive divider from the internal switch resistance and the 50 Ω, due to the fact that the switches open sooner then the actual rise time. This cuts the pulse amplitude by 38%. We can calculate this by taking the ratio of the switch "close time" to the rise time and multiply that by the maximum potential from the resistive divider.

21

3.2.2   Transmission Line Circuit Model

General two-wire transmission lines can be used everywhere in the lab and a segment of transmission line connects the high-voltage modulator to the induction cell. The type of transmission line used is RG-58 coaxial cable. Such a transmission line can be modeled as a differentially lumped circuit distributed along the length of the transmission line as shown in [Fig 3.9]. For a differential length Δx, the elements that make up the model are two series elements, the resistance per unit length and inductance per unit length and the shunt element is the capacitance per unit length.
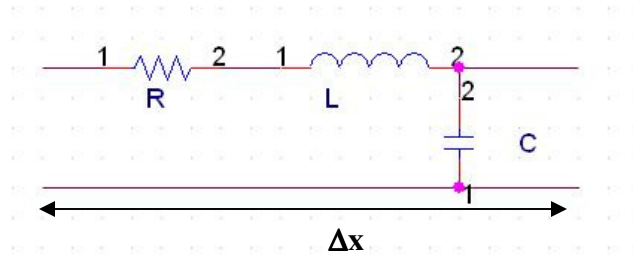
Fig 3.9. Transmission line circuit model [19]

For a coaxial transmission line, the formulas for capacitance and inductance per unit length are derivable from Maxwell's equations 3.3 and 3.4 respectively [19].

$$C = \frac{2\pi\varepsilon}{\ln\left(\dfrac{b}{a}\right)} \tag{3.3}$$

$$L = \frac{\mu}{2\pi}\ln\left(\frac{b}{a}\right) \tag{3.4}$$

Where a, is the radius of the inner conductor and b is the radius of the outer conductor.
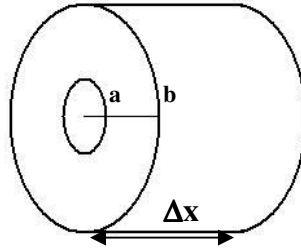
Fig 3.10. Coaxial Transmission Line (cross-sectional view)

The resistance term is usually measured since it depends on the material used for the center conductor and if the center conductor is stranded or solid. The measured values for RG-58 as given from BELDEN are displayed in table 3.2.

Table 3.2. RG-58 Specifications [20]

Parameters	Values
Capacitance/Δx	30.8 pF/ft
Inductance/Δx	0.077 µH/ft
Resistance/Δx	10.8 Ω/1000ft

The impedance of the cable can be calculated using eqn. 3.5, which for the specifications listed, is 50 Ω.

$$Z_o = \sqrt{\frac{L}{C}} \tag{3.5}$$

3.2.3   Induction Cell Circuit Model

The induction cell is the same circuit as the wall current monitor, a parallel RLC circuit, except for the modification to the resistance term. The resistance term is modified so that when a segment of transmission line is connected between the modulator and the cell, the pulse will be properly terminated. The resistance term of the cell was changed to 50 Ω. This changes the poles of the circuit and equivalently

23

its band of operation. The bode plot of the pass-band range is reduced from that of the wall current monitor.
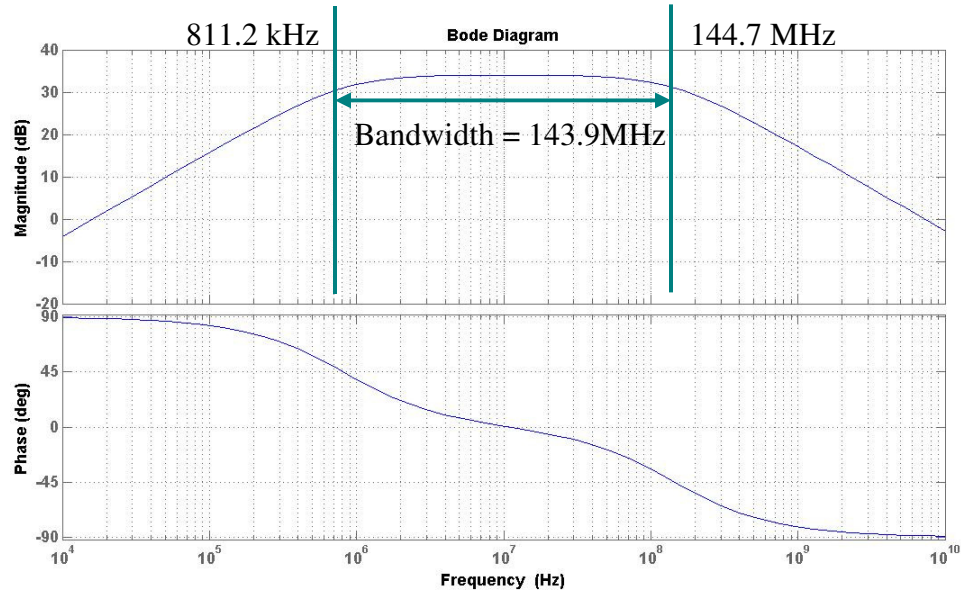
Fig 3.11. Bode plot of circuit model (R = 50 Ω, L = 9.81 µH, C = 22 pF)

This modification changes the low frequency pole to 811 kHz and the high frequency pole to 144 MHz which will modify the measurement of the beam current and in turn limit the use of the induction cell as a wall current monitor. The calculated droop of the detector will be 40% for the 50 Ω resistor which is extremely poor for a wall current monitor capturing a square beam current pulse. The reduction in the pass-band width also limits the frequency of the signal applied to the induction cell which is critical for the applied pulsed fields. The pulse width of the fields is 15 nsec, taking the gaussian pulse as a half period sine wave, then the frequency content of the applied signal is 33 MHz which is in the pass-band of the device.

3.2.4 Entire Circuit Model

The entire circuit [Fig. 3.12] consists of the modulator, the induction cell and a segment of transmission line connecting the two.
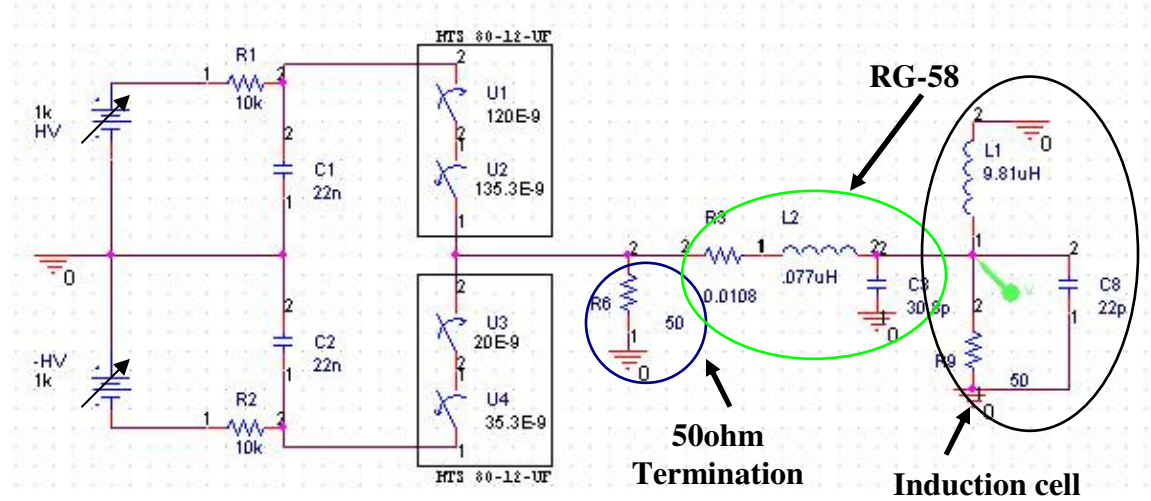
Fig 3.12. Entire circuit model in pspice

Each section of the circuit is outlined with circles and labels. There is an additional component that has been added and not yet described, the 50 Ω resistor before the segment of RG-58. Before simulating the circuit in pspice, we will explain the reason for the additional resistor.

After the modulator fires and a pulse is sent down the transmission line, the current then splits up into the three elements of the parallel RLC circuit of the induction cell. When the modulator turns off, an induced pulse is reflected back up the transmission line to the modulator which is "off" by that time and so the pulse will reflect again back down the transmission line because of the high impedance open-state of the BEHLKE switches since $\Gamma = \dfrac{Z_L - Z_O}{Z_L + Z_O} = \dfrac{1Meg - 50}{1Meg + 50} \approx 1$. So a 50 Ω resistor is placed at the entrance point of the transmission line so that the pulse reflected back from the induction cell up the transmission line is terminated.

Now we can perform a PSpice simulation of the whole circuit allowing enough time for both HTS circuit models to send a pulse. The simulation output along with the real circuit output is displayed in figure 3.13 below as the voltage across the 50 Ω resistor inside the induction cell.
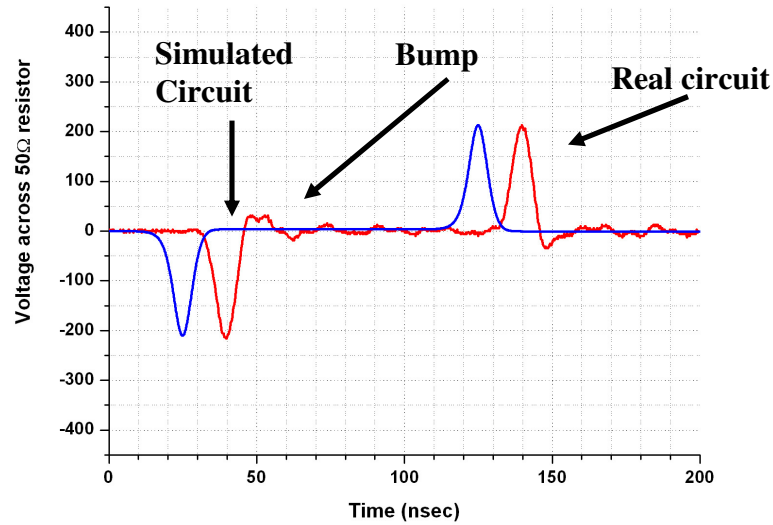
Fig 3.13. Simulated and real voltage across 50 Ω resistor inside induction cell

The simulation results compare very nicely with the real circuit performance. The amplitude has decreased from 364 volts in figure 3.8 to 210 volts with the additional components attached for a 1kV charge on the modulator capacitors.

The one feature of the real circuit that was not seen in simulation was the bump in the output waveform. This will be important for ear-field focusing, because the beam bunch will have to fit inside the ear-fields and so any "noise" or improper terminations of the initial decelerating pulse would affect the beam. This bump in the real circuit output seems to be an under-damped response of either the coax cable or the induction cell or a combination of the two. The measured damping coefficient from the plot is approximately 60 nsec. If we assume the switches are off so they are

26

at a high impedance state, we can disconnect the transmission line and induction cell

from the rest of the circuit. Taking the pulse frequency to be 33 MHz and calculating

the impedance of the circuit, we get from MATLAB $Z = 25.8289 - 3.1574 j$. The real

part of the impedance comes from the two 50 Ω resistors in parallel and the

imaginary part is the equivalent capacitance since its negative. The calculated

equivalent capacitance is 1.52 nF. If we use the damping coefficient of a parallel RLC

circuit, $2RC$, then the calculated time constant is 76.3 nsec. This agrees with the

measured value.

3.3   Design Considerations and Limitations

This section describes the saturation limits of ferrites in terms of the volt

second product and how the circuit operates to prevent saturation of the material as

well as why the specific material was chosen. We also review and calculate the power

dissipated in the ferrite and suggest methods to what could be done to minimize

power dissipated. The section ends with a calculation of the inductance of the ferrite

toroid.

The modulator source drives a current density around the ferrite toroid,

creating a time varying magnetic field intensity inside the toroid equal to $\vec{H} = \dfrac{\vec{J}A}{2\pi r}$.

Because of Lenz's law, we will have an equal and opposite current generated to

oppose the change in flux, the induced current. The time varying magnetic field will

also induce an electric field or a voltage drop across the gap from faraday's law. What

limits the ability to induce a voltage drop across the gap is the $\dfrac{d\vec{B}}{dt}$ term. If this term

goes to zero, we have the electrostatic condition, namely $\nabla \times \vec{E} = 0$. This means that the curl or the sum of all voltages around the loop, thinking in terms of circuit theory, is zero.
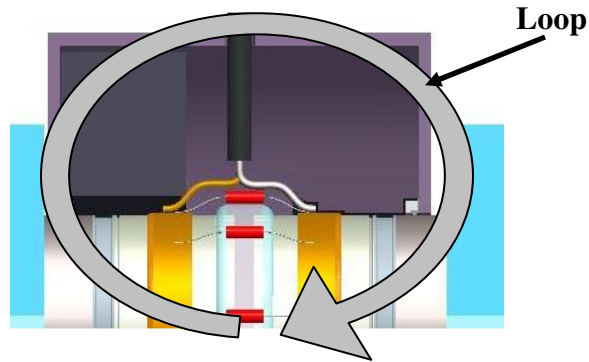
Fig 3.14. Curl of electric field within the induction cell

The point at which this term goes to zero is at the top of the hysteresis curve, the saturation point or B_S, where the magnetic flux density does not change anymore with a change in magnetic field intensity. To calculate the limit, use eqn. 3.6,

$$\Delta V \Delta t = \Delta B A \qquad (3.6)$$

where the $\Delta V \Delta t$ is the volt-second product, which is the applied pulse voltage to the

core multiplied with the pulse rise-time. The cross-section area of the core, and ΔB

gives the change in magnetic flux. The ferrite is picked based on a material with a B_S

well above the typical flux swing of the circuit so saturation does not happen easily.

For the ferrite material used in UMER, CMD5005, the saturated magnetic flux

density is 3200 gauss [21]. The pulse rise-time from the modulator is 8.8 nsec and the

cross-sectional area of the core is 22.82 cm^2. The largest beam current of 104 mA will

require the largest focusing field, 1.4893 kV [see section 3.5] so the change in

magnetic flux will be 57.4 gauss per pulse.

After applying a pulse to the ferrite core, it needs to be reset so that we don't

work the material up the hysteresis curve and into saturation. Typically a negative

pulse in the form displayed in figure 3.15 is applied in the reverse direction from the

initial pulse to drive the material back down the hysteresis curve [22]. This can also

decelerate the beam coming through the induction cell if the modulator that supplies

the negative pulse is triggered while the beam is still in the induction cell.
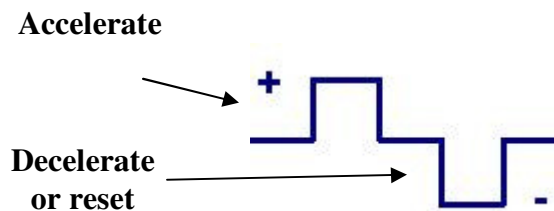
Fig 3.15. Pulse configuration that supports core resetting

The power loss in the material must also be considered with ferrites because

the joule heating could lead to the material reaching the Curie temperature which

would render it useless as a ferrite. The CMD5005 has a curie temperature of 130 °C [21].

The loss can be traced using the loss curve for the given material where the bottom axis of the plot is the rise-time of the pulse applied in microseconds for full saturation. The vertical axis is the loss in J/m^3. Since we have a field of 57.4 gauss in the ferrite for a pulse rise time of 10 nsec, then the approximate time it would take to reach full saturation for CMD 5005 would be 557 nsec, using the saturation flux density 3200 gauss. So the loss in the ferrite would be approximately 110 J/m^3 for full flux swing to the saturation point of the material. The volume of the ferrite is 0.000347 m^3 so the loss would be 38.2 mJ.
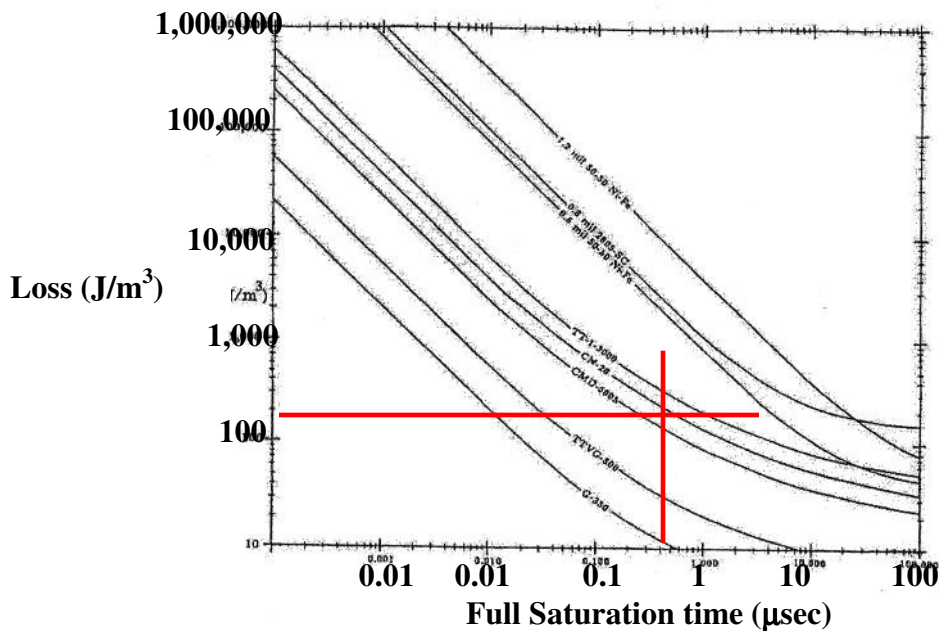
Fig 3.16. Power loss curve for CMD 5005 and other materials [22]

A way to minimize this loss would be to slow the rise time of the pulser.
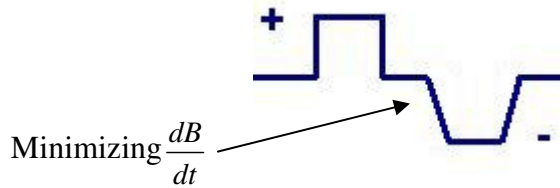
Fig 3.17. Reset pulse with minimized $\frac{dB}{dt}$

Since it takes longer for the material to switch from one state to the other, the change in magnetic flux stayed the same but the rise time increased. A longer rise time means there is less J/m^3 loss in the material using the loss curve. In the limit, if the signal was DC, then the dipole moments in the material would not reorient themselves and so no energy would be loss in the ferrite. The loss would be in the DC power dissipated in the wire wrapped around the ferrite.

The inductance of the ferrite material is also a key factor in the choice of ferrite, which brings us to the permeability of the material. The initial permeability of the ferrite specified from CMI, is 1300 [21]. To calculate the inductance of the ferrite toroid, we can use the formula for the coax cable, eqn. 3.4. The outer radius of the toroid is 6.6 cm and the inner radius is 3.0 cm. The height of the material is 3.1 cm, so the calculated inductance of the toroid is 7.93 µH and the measured value used in the simulations and other calculations is 9.81 µH. To measure the approximate inductance due to the ground loop through the cluster plate, we divide by the initial permeability of the ferrite using the ferrite as an amplifier. This is 7.5 nH.

3.4   Transverse Effects from the Induction Cell

In this section we relate the potential drop across the glass-gap to the potential inside the beam pipe in the vicinity of the gap region. This allows us to study the

transfer matrix of the induction cell and its focusing component. In section 3.4.1, we examine the validity of the electrostatic solution in comparison to the electromagnetic problem. In section 3.4.2, we calculate the on-axis potential and in section 3.4.3 calculate the radial component of potential. Finally in section 3.4.4 we will compare the focusing strength of a UMER quadrupole to the focusing strength of the induction cell; even though the elements are different, this gives the relative difference between the focal lengths of each device.

3.4.1   Validity of Electrostatic Solution

In order to view the similarities, we must draw both problems. In the top figure we have the ferrite material loaded inside a cavity which shorts either side of the gap that is a distance S. The curl of the electric field is zero at DC, i.e. the gap is shorted and in the time varying case as long as there is a $\dfrac{d\vec{B}}{dt}$ term from the ferrite because of the current loop around the ferrite, then we can induce the voltage across the gap. This can be equivalent to having two separate conductors that are not tied together by a cavity as long as $R \gg S$, $l \gg R$ and $h \gg R$ [23].

$$\int \frac{dB}{dt} ds$$

$$\Delta V = -\int \frac{dB}{dt} ds$$
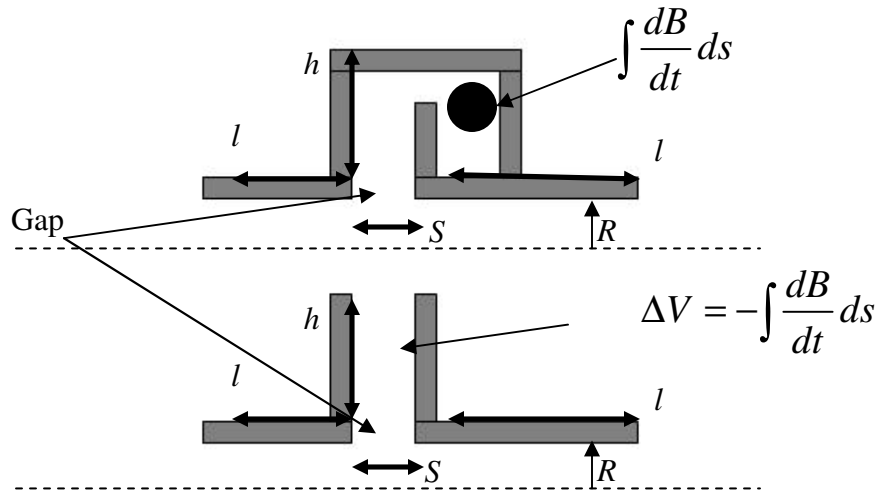
Fig 3.18. Electromagnetic problem versus electrostatic problem

The voltage induced across the gap is just ΔV, as long as were concerned only with the electric field near the gap and not at the back wall of the cavity or near the ferrite material.

3.4.2 On-axis Potential

The field lines within the induction cell can be calculated using Laplace's equation in cylindrical coordinates in the form shown below with no potential variation in the theta direction. The geometry of the problem is outlined in section 3.1, figure 3.1. Because of the argument in section 3.4.1, this is a purely electrostatic problem with two different pipes each with a radius of R and separated by a negligible distance with a potential drop across them, i.e. the bipotential lens. This solution also ignores beam loading and so the self fields of the beam are ignored.

Using separation of variables with a solution of the form $\phi(z,r) = F(z)G(r)$ and appropriate boundary conditions, we obtain a solution for the on-axis potential eqn. 3.7 [24, 25].

$$\varphi(z) = \frac{V_2 + V_1}{2} + \frac{V_2 - V_1}{2} \tanh\left(\frac{1.32}{R} z\right) \qquad (3.7)$$

For a potential difference across the gap ($\Delta V = V_2 - V_1$) and using $V_2 = 100$ volts,

$V_1 = 0$ volts and $R = 2.54$ cm we get a plot of the on-axis potential.
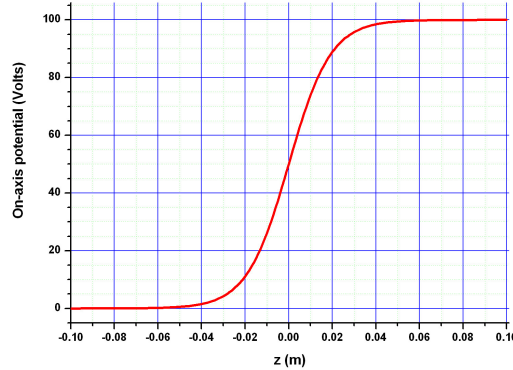
Fig 3.19. On-axis $(r = 0)$ potential

3.4.3 Radial Component

If we look at the potential off-axis, there will be a radial-dependent potential

term that will focus the beam transversely as well as accelerate the beam as it exits

the lens of the induction cell. If we substitute a power series expansion of the form

$\varphi(z,r) = \sum\limits_{n=0}^{\infty} a_n(z) r^{2n}$ into Laplace's equation and take the necessary derivatives, we

obtain eqn. 3.8 [24, 25].

$$\varphi(z,r) = \sum\limits_{n=0}^{\infty} \frac{(-1)^n}{(n!)^2} \varphi^{2n}(z,0) \left(\frac{r}{2}\right)^{2n} \qquad (3.8)$$

Writing out the first three terms of the expansion and calculating the on-axis

derivatives, a contour plot of the solution is displayed in figure 3.20.

34

If we look at the contour plot, any particles traveling in the center of the acceleration gradient will not experience a radial component. When the particles are in the edges of the fields, there will be a component in the radial direction that will distort the beam size in the transverse plane.
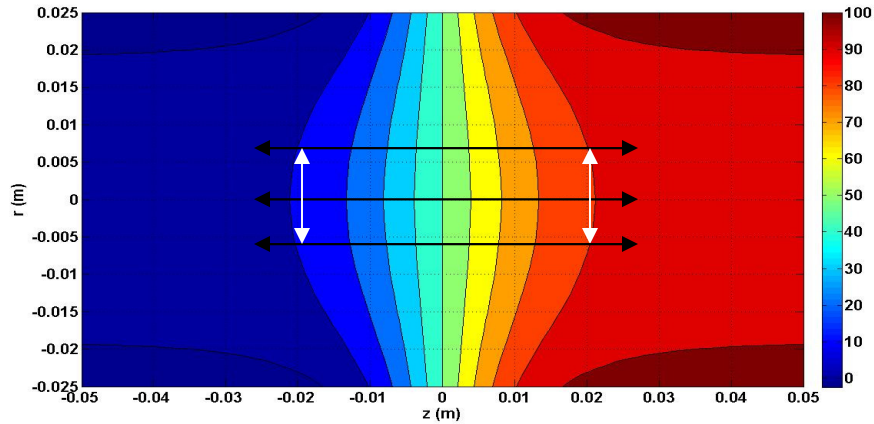
Fig 3.20. Contour plot of potential

Since the derivation assumes the pipe's separation distance d is small in comparison to the pipe radius, so that the lens is narrow, the potential variation is fairly constant over a radius of 5 mm with a variation of 2.3%, assuming the beam is in the center of the induction cell and is laminar. So for all the beams that could be launched into the UMER lattice, only the 104 mA and 78 mA beams will experience a non-planar longitudinal accelerating gradient, assuming the quadrupoles are operating at there nominal current of 2.21 A.

3.4.4   Beam-Optics Transfer Function

The focal lengths for the various focusing fields can be calculated using eqn. 3.9 [24, 25].

$$\frac{1}{f_i} = \frac{3}{8}\left(\frac{1.32}{b}\right)\left(\frac{\varphi_o}{\varphi_i}\right)^{\frac{1}{4}}\left(\frac{\varphi_o + \varphi_i}{\varphi_i - \varphi_o}\log\frac{\varphi_i}{\varphi_o} - 2\right) \qquad (3.9)$$

The potential φ_i is in the image plane, φ_o is in the object plane of the induction cell and b is the beam pipe radius. So the pipe in the object plane would be held at potential V_2 and the pipe in the image plane would be held at V_1.

The transfer matrix in the thin lens approximation has the form of $\begin{pmatrix} 1 & 0 \\ -\dfrac{1}{f} & 1 \end{pmatrix}$,

where f is defined as the focal length of the focusing element. For a quadrupole in UMER the focal length is 0.158 m using the thin-lens approximation $\dfrac{1}{f} = \kappa l_{eff}$ [5].

κ for a magnetic quadrupole is defined as $\kappa = \dfrac{qB_0}{\gamma mav_0}$, where B_0 is the integrated gradient, q charge of an electron, γ the Lorentz factor, a the diameter of the quadrupole aperture, m the mass of an electron, v_0 the velocity of the beam and l_{eff} is the effective length of the quadrupole [5]. The peak integrated field per amp for the quadrupoles in UMER is 13.438 G/A where the operating current in the quadrupoles is 2.21 A [26]. The effective length of the quadrupoles is 3.72 cm [26].

Before we can calculate the focal length of the induction cell, we need to calculate ΔE the ear-field energy required for any of the UMER beams using eqn. 3.10,

$$\Delta E = \frac{1}{2}m\left(2C_s + v_0\right)^2 - \frac{1}{2}mv_0^2 = 2mC_s\left(v_0 + C_s\right) \qquad (3.10)$$

where C_s is the sound speed [refer to section 2.1] and m the mass of an electron. The ear-field energy is the energy spread from the main beam energy due to head and tail expansion. The head of the beam is accelerated from the main beam and the tail of the

beam is decelerated from the main beam. To calculate the correct C_s for each of the

beam currents, the average radius must be properly calculated without neglecting

space-charge or the operating point of the quadrupoles [refer to section 4.1.1]. The

focal length for the induction cell is then calculated with eqn. 3.9 where $\varphi_o = E_{beam}$ the

main beam energy and $\varphi_i = E_{beam} - \Delta E$ is the main beam energy minus the ear-field

strength for a decelerating ear-field. To calculate the focal length for an accelerating

ear-field, $\varphi_i = E_{beam}$ and $\varphi_o = E_{beam} - \Delta E$. The calculated focusing strengths and focal

lengths for all beam currents are displayed in table 3.3, assuming the quadrupoles are

operating at full current.

Table 3.3 Ear-field strengths and focal lengths

Beam Current	Average Radius	C_s (m/s)	$E_{beam} - \Delta E$	Beam Tail - Accelerating Focal Length (m)	Beam Head - Decelerating Focal Length (m)
0.7 mA	1.44 mm	2.97E5	9.7987keV	740.7	748.3
7.0 mA	3.06 mm	8.06E5	9.4485keV	94.3	97.0
23 mA	4.70 mm	1.31E6	9.0995keV	33.8	35.4
78 mA	8.24 mm	1.96E6	8.6313keV	13.7	14.7
104 mA	9.40 mm	2.13E6	8.5107keV	11.4	12.3

As the beam current increases, the sound speed increases and so the required focusing

field increases and the focal length of the induction cell decreases. The induction cell

is a weak focusing element for any beam current in comparison to the quadrupoles

short focal length. At the shortest focal length, the induction cell is still a factor of 72

greater then the quadrupoles.

Chapter 4: Energy Modulations

This chapter reports on the first attempts to use an induction module to deliberately place energy modulations on the flat top region of the space-charge dominated beam propagating within the UMER lattice. The purpose of the experiment is to verify that an initial energy modulation converts into a density modulation as predicted by the cold fluid model. The conversion of energy modulations to density modulations is analogous to the conversion of density modulations into energy modulations [4]. In section 4.1 the experimental setup is described, In section 4.2, the results of the initial perturbation experiment are compared to the one-dimensional cold fluid model.

4.1   Experimental Procedures

In this section, the experimental setup is described. The layout of the UMER ring and its parameters as well as the diagnostics used, namely the Beam Position Monitors (BPM) [27] and the wall-current monitor [refer to section 3.1] is reviewed in section 4.1.1. The timing of the experiment is outlined in section 4.1.2.

4.1.1   Hardware and Experimental Setup

The schematic of the University of Maryland Electron Ring (UMER) is displayed in fig. 4.1.
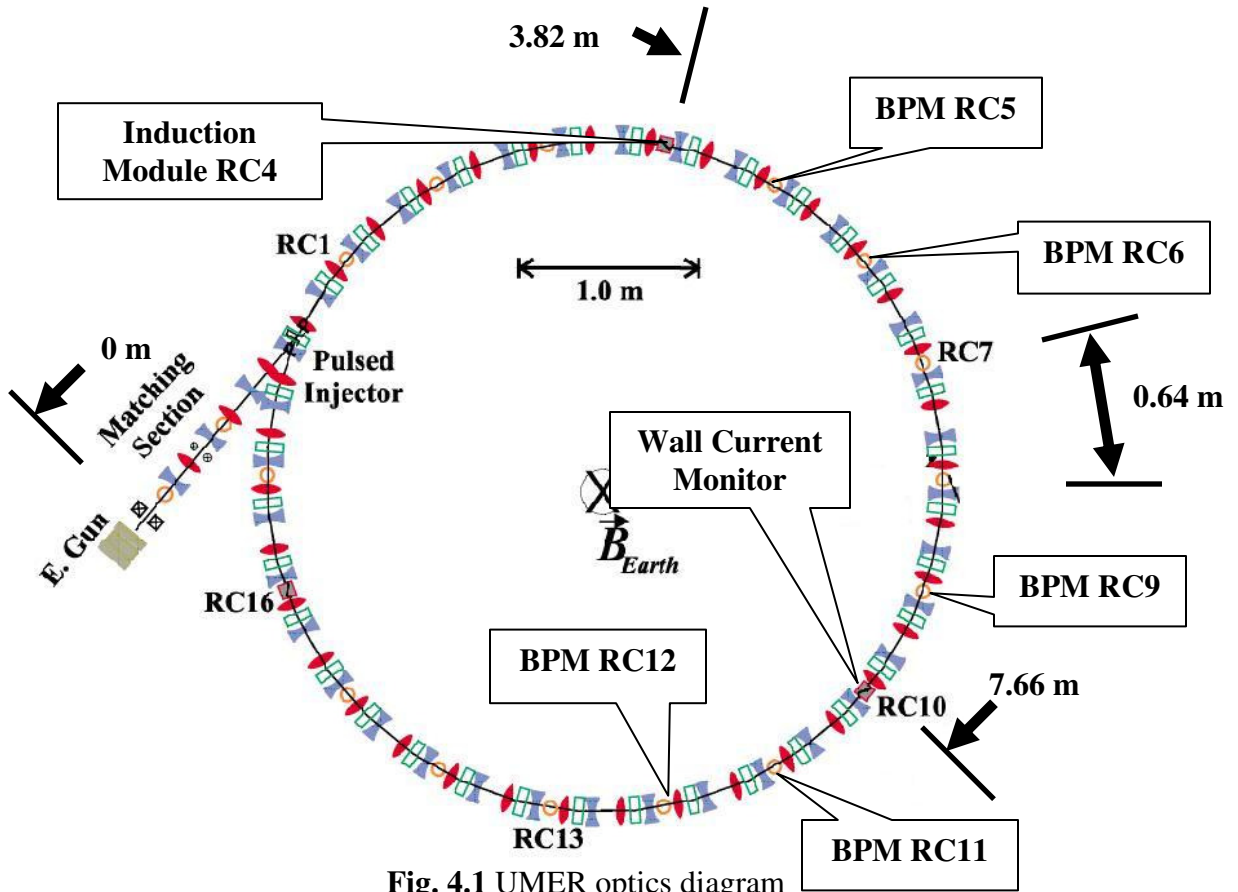
Fig. 4.1 UMER optics diagram

The beam is born from a dispenser cathode in a Pierce-type electron gun with an anode grid [28].

Table. 4.1 UMER system parameters

Beam Energy	10 keV
$\beta = v/c$	0.197
Pulse Length	20-100 ns
Ring Circumference	11.52 m
Lap Time	197 ns
Pulse Repetition Rate	15-60 Hz
FODO Period	0.32 m
Zero-Current Phase Advance, σ_0	76^0
Zero-Current Betatron Tune, ν_0	7.6
Tune Depression	≥ 0.2

An aperture wheel immediately downstream of the electron gun anode is used to aperture the full 10 mm beam, resulting in various beam currents with the same initial transverse current densities.

Table. 4.2 Aperture radius and beam current exiting the gun

Aperture Radius	Beam Current
0.25 mm	0.7 mA
0.875 mm	7.0 mA
1.5 mm	23 mA
2.85 mm	78 mA
Full Beam	104 mA

The 1.4 m injection/matching section has a solenoid and six quadrupoles after the electron gun. The injected beam current is measured using a Bergoz FCT-082-20:1 fast-current transformer located in the injection line after the second quadrupole [29].

Once the beam is injected into the ring, the quadrupole focusing lattice contains the beam transversely. Table 4.3 shows the calculated average radius for each beam current with the quadrupoles operating at their nominal operating current of 2.21 A and at 83% of the nominal operating current.

Table. 4.3 Average calculated radius in ring [30]

Beam Current	ε (μm) un-normalized	Average Beam Radius @ 100%	Average Beam Radius @ 83%
0.7 mA	7.6	1.44 mm	1.64 mm
7.0 mA	25.5	3.06 mm	3.58 mm
23 mA	39.0	4.70 mm	5.66 mm
78 mA	86.6	8.24 mm	10.06 mm
104 mA	97.3	9.40 mm	11.51 mm

With a lattice periodicity S equal to 0.32 m and a zero-current phase advance σ_0 of

76^0, the betatron oscillation wavelength λ_0 is equal to 1.51 m using $\lambda_0 = \dfrac{2\pi S}{\sigma_0}$ with no

space-charge [5].

When we have space-charge, the betatron wavelength increases to λ and is

defined by eqn. 4.1,

$$\lambda = \frac{2\pi}{k} = \frac{2\pi S}{\sigma} \tag{4.1}$$

where k is the wave number and σ is the phase advance with space-charge. To

calculate the phase advance with space-charge, we can use the smooth approximation,

$$\sigma = \sigma_0 \left(\sqrt{1 + u^2} - u \right) \tag{4.2}$$

where u is a parameter defined as $u = \dfrac{KS}{2\sigma_0 \varepsilon}$ [5]. The variable K is equal to the

generalized perveance and ε is the un-normalized emittance.

$$K = \frac{2I}{I_0 (\beta\gamma)^3} \tag{4.3}$$

Here the characteristic current I_0 is equal to 17 kA for electrons, I is the beam

current, β is the ratio of the beam velocity to the speed of light and γ is the Lorentz

factor. For the 23 mA beam, the wavelength with space-charge is 3.55 m, where the

phase advance with space-charge is 32.4^0 assuming the quadrupoles are operating at

100% of their normal operating current.

To calculate the average radius $\bar{R}$ shown in table 4.3, for a periodic focusing channel with space-charge we can use eqn. 4.4, again using the smooth approximation [5].

$$\bar{R} = \bar{R}_0 \sqrt{u + \sqrt{1+u^2}} \tag{4.4}$$

$\bar{R}_0$ is the average radius without space-charge and u is the same parameter as defined earlier.

The induction module [refer to Ch. 3.2-3.3] is installed at RC4 which is 3.82 m from the gun and the wall-current monitor is installed at RC10, 7.66 m from the gun.

The BPMs are used to monitor the beams transverse centroid position as well as current profiles.

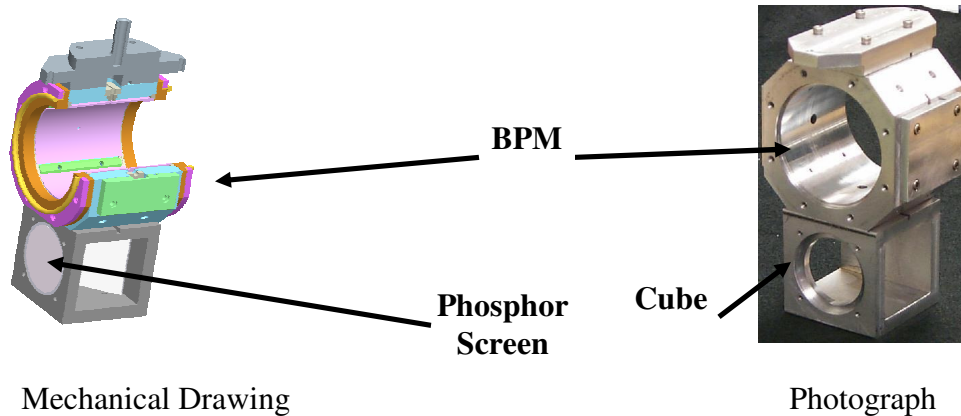Mechanical Drawing   Photograph
Fig. 4.2 BPM and phosphor screen

A cube containing a mirror and phosphor screen is mounted underneath the BPM in order to perform first-turn transverse measurements. When the BPM is inserted into the beam path, a charge is induced on one of the electrodes equal to eqn. 4.5 [31, 32].

$$Q = \frac{\Phi L}{2\pi v_o} I \tag{4.5}$$

$$C = \frac{\Phi \varepsilon_0 L}{\ln\left(\dfrac{b}{a}\right)} \tag{4.6}$$
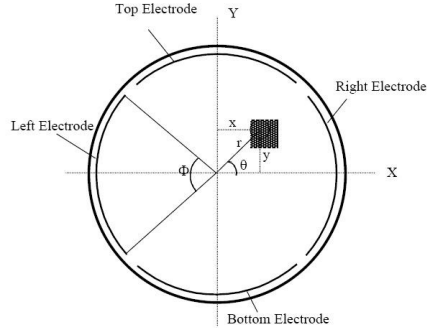

Fig. 4.3 Electrode schematic [31]

In the electrode schematic, the capacitance between the electrode and beam pipe is given by eqn. 4.6. Here a is the radius of the electrode and b is the radius of the beam pipe. The length of the electrode out of the page (z-axis) is given by L, the angular segment of each electrode is given by Φ, relative permittivity in vacuum is ε_0, and beam current is I. The distance between adjacent BPMs in the ring is 0.64 m from center to center, therefore the BPM in RC5 is 4.46 m away from the gun.

The high voltage modulator is located right next to the cell itself along with a digital delay generator for TTL level signals. An Agilent oscilloscope is used for digitizing the voltage waveforms sent to the cell and the reference timing information from the BPM at RC3. A Tektronix oscilloscope is used to digitize the voltage output from the wall current monitor and the BPMs in the experiment.
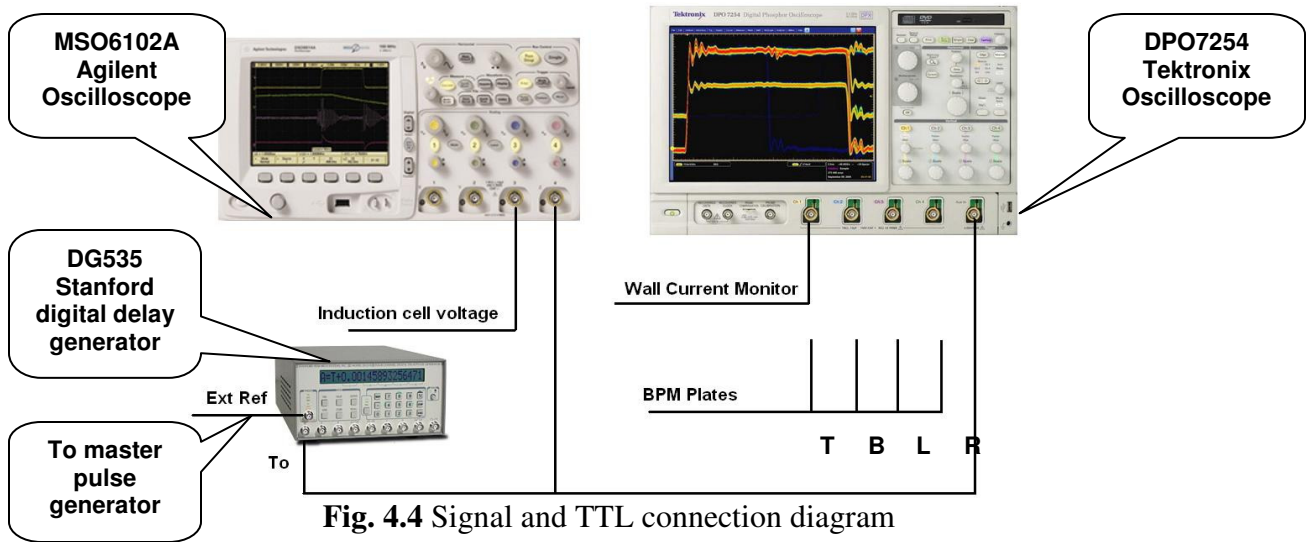
Fig. 4.4 Signal and TTL connection diagram

The purpose of the Stanford Generator is to branch off the single pulse coming from the master pulse generator to both of the HTS switches individually. This allows the ability to adjust the time between the positive and negative pulses applied to the induction cell. If both pulses are set with a given width between each other, then the master pulse generator can be used to adjust the phase delay between the time at which the modulator is pulsed and where the beam is located in the ring at a given time.

4.1.2   Timing

Timing is important during the experiment because the only measure of the beams location prior to the induction cell is the BPM in RC3. The amount of time it takes for the 10 keV beam to propagate from RC3 to the induction cell is 10.94 nsec.

Negative Perturbation

Fig. 4.5 Simple timing diagram

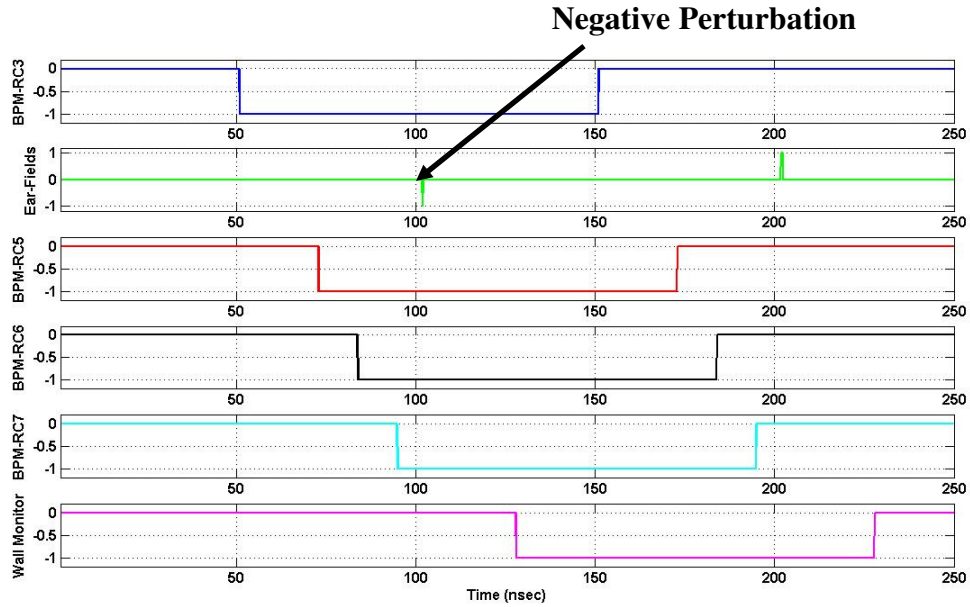The timing diagram displays the time where the beam should be located from chamber to chamber. Either the positive or negative ear-field could be placed in the middle of the beam by adjusting the phase delay of the master pulse generator, though the diagram is shown with the negative ear-field placed in the middle of the beam. Both pulses must be always on to reset the ferrite continuously as discussed in section 3.3.

4.2 Experimental Data

In this section, we present results of the experiment and compare to the one-dimensional cold-fluid simulation so that we can understand what is happening to the perturbation. Initially in section 4.2.1, we apply a perturbation with the induction cell on the 23 mA beam to understand how the perturbation is evolving from an initial energy perturbation to a density modulation with the use of the one-dimensional fluid model. In section 4.2.2, the perturbation experiment will be repeated but this time

allow the beam and waves to propagate for over 60 m so that the waves can fully

separate. From this we can compare the experimentally measured sound speed with

the corresponding theoretical value. We also report on the steepening of the waves

due to the acceleration/deceleration of the electrons in the tip of the wave itself.

4.2.1 Initial energy perturbation experiment

The waveform applied to the induction cell, that is used to perturb the beam

has a FWHM of 8.8 nsec.

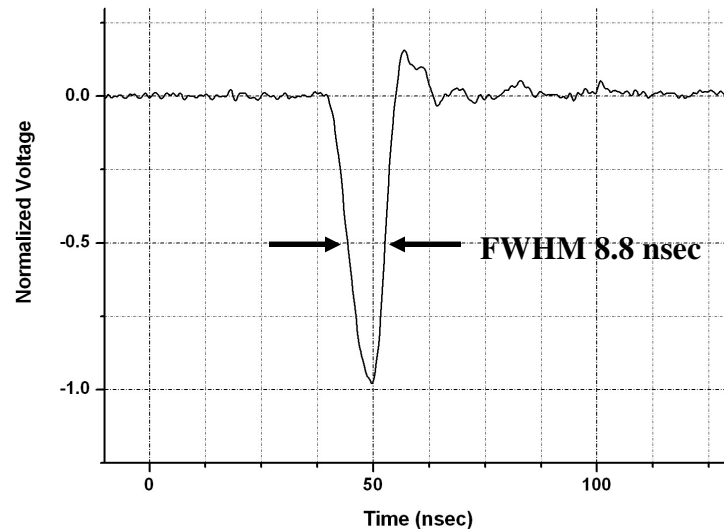**Fig. 4.6** Normalized *negative* perturbation

The magnitude of the perturbation applied to the 23 mA beam was 300 V. The

voltage induced on the BPM plates was then captured using an oscilloscope, from

BPMs RC5 to RC13. The quadrupoles in the ring were powered at 100% of their

normal operating current, which is a factor for the beam size and the theoretical

calculations of sound speed of the 1-D code.
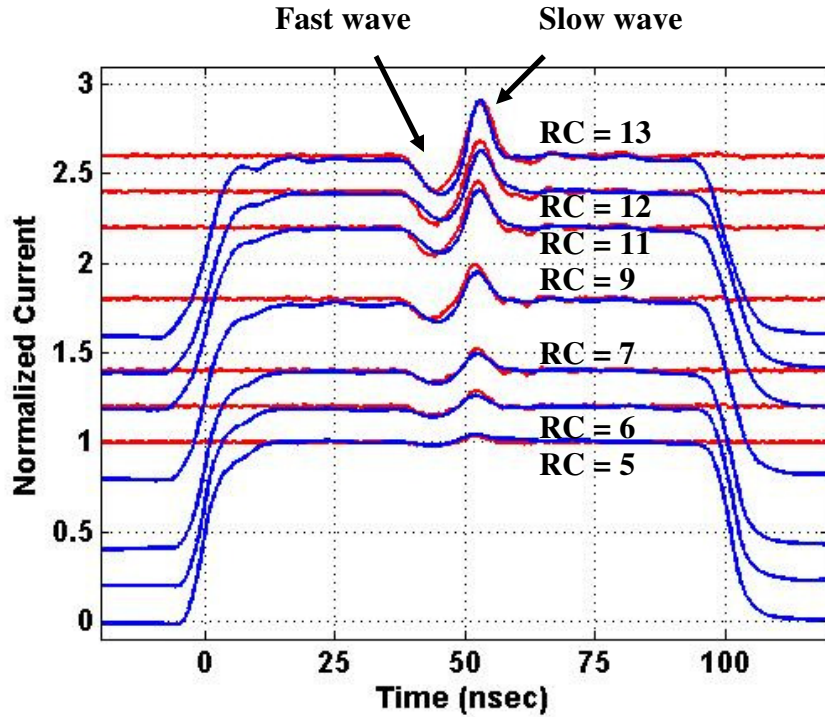
Fig. 4.7 Results of *negative* 300 V perturbation experiment and 1-D code

In Fig 4.7, the blue curves in the mountain range plot are the normalized integrated signals from the BPMs and the red curve is the simulation of the space-charge waves from the one-dimensional fluid code. The red curves do not represent the beam ends seen in the experimental results since the 1-D space-charge wave model ignores the eroding beam ends. In this simulation, the ratio of current perturbation to beam current, η, was equal to zero. The ratio of the velocity perturbation to the velocity of the beam, δ, was equal to 0.173 assuming the average beam size in the ring was 4.53 mm and the actual measured beam current was 20.72 mA.

As the beam and the perturbation continue on from chamber to chamber, the difference in peak-to-peak current of the perturbation increases. This increase arises from the summation of the overlapping fast and slow waves. If two Gaussian pulses

47

with opposite polarity are directly on top of each other, there sum is zero. Once these

pulses begin separating, the one pulse begins to move in the forward direction and the

other in the backward direction and there sum is non-zero, (see Fig. 4.8). Once the

pulses had fully separated, the peak-to-peak amplitude of the resulting sum is equal to

the sum of the fast wave magnitude and the slow wave magnitude.
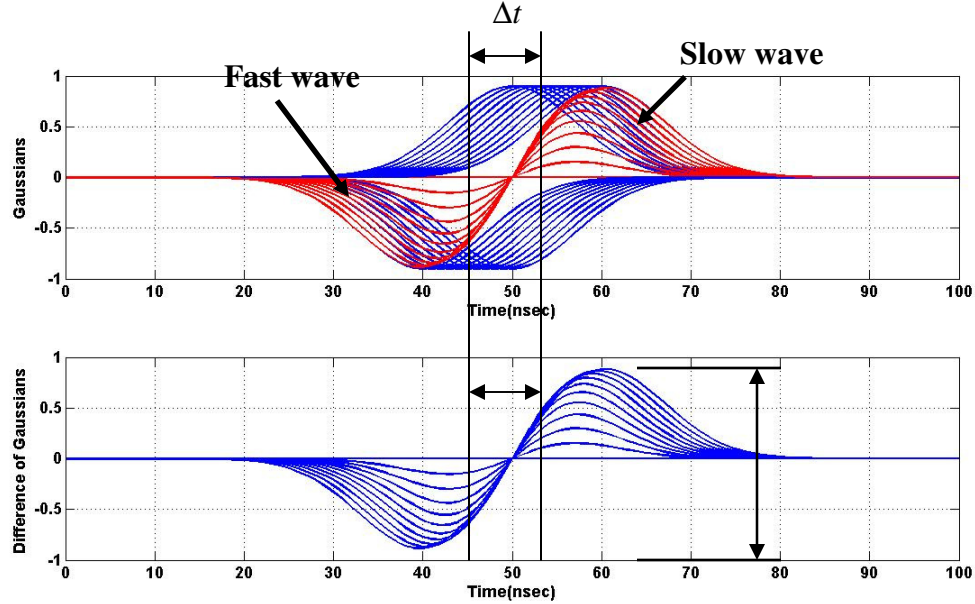
Fig. 4.8 Difference of Gaussians

A difficulty arises in measuring the time separation (Δt) of the peaks during the

increase in the wave amplitude, until each of the waves has fully separated and the

amplitude is at its peak. This will impact the experimentally measured C_s as described

later in section 4.2.2. The simulation results for this particular experiment agree well

with the experimental results.

The perturbation experiment and simulation was repeated with a perturbation

of opposite polarity.
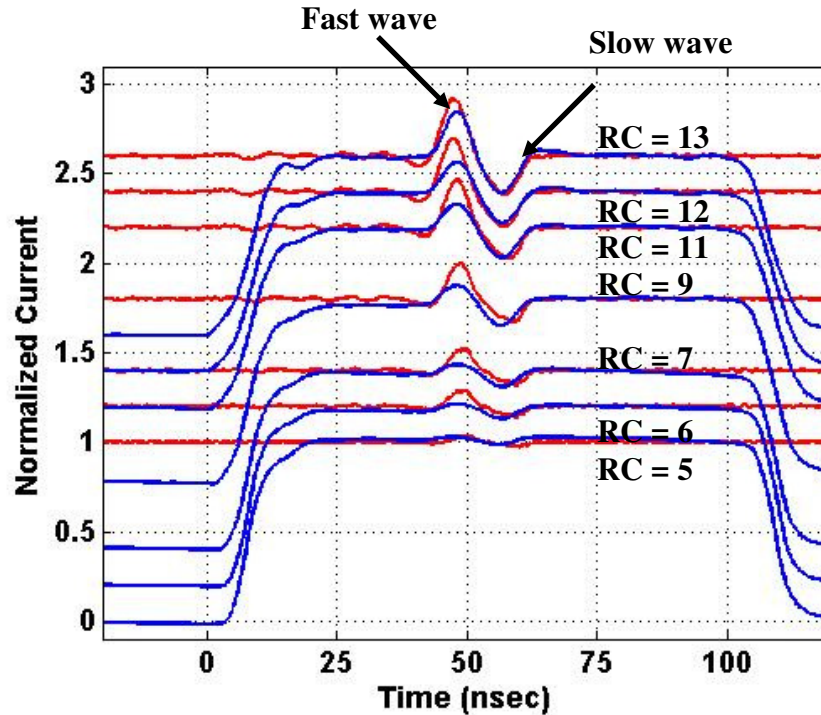
Fig. 4.9 Results of *positive* 300 V perturbation experiment and 1-D code

With the negative perturbation experiment as well as the positive, the energy

perturbation appears as a current modulation by RC5 and the amplitude of the pulse

continued to grow because of the wave separation, however, with a positive

perturbation, the wave polarities flip in current space. For the simulation of this

experiment, the ratio of the velocity perturbation to the sound speed for this

experiment was equal to 0.173 and the average beam size as well as beam current and

the value of η was the same as in the previous experiment.

A comparison of Figs. 4.7 and 4.9 shows that in the case of the positive

perturbation, the simulation does not agree as well with the experiment as in the case

the negative perturbation experiment. The possible reason for this may have to do

with scraping of the fast wave against the beam pipe, which may be similar to what

was exhibited in reference [33] by Kai Tian.

The experimental widths of both the fast and slow waves are very close to the cold-fluid simulation but the amplitude of the fast wave does not agree as well as the slow wave with the cold-fluid simulation results. Since there is more charge in the region of the fast wave, the beam size will grow. Coupled with this is the fact that the waves carry a velocity modulation with them that is different from the main beam energy. The dispersion function associated with the lattice elements will shift the centroid of the perturbation from the main beam. So if the main beam is closer to one side of the pipe then the other within the induction cell, this will result in a polarity dependent perturbation loss mechanism. Scraping against the beam pipe resulting in a loss of current within the fast wave for a positive perturbation as seen in figure 4.9 but for negative perturbations, there will be no scraping of the slow wave as seen in figure 4.7.

4.2.2   Energy perturbation experiment over a long path

Using the ability of UMER to transport current over long distances, we can examine the waves propagate on the main beam from turn to turn while experimentally measuring the sound speed and comparing that to the theoretical value defined in section 2.1 [eqn. 2.3].

We can calculate the speed of the wave in the beam by measuring the time separation of the peaks (Δt) after traveling a distance Δz from the point of application of the perturbation:

$$v_0^2 - C_s^2 = \frac{2\Delta z}{\Delta t} C_s \qquad (4.7)$$

solving the quadratic equation 4.7 for C_s, we obtain the sound speed.

During this experiment, a negative 50 V energy perturbation was placed on the flat-top region of the 7 mA beam. The perturbation converted into a current modulation and back into an energy modulation and continues to oscillate back and forth eventually splitting into fast and slow waves. The quadrupoles for these experiments are operating at 83% of their nominal value. Fig 4.10 was created by taking the current profile from the wall current monitor at subsequent laps of the beam, every 197 nsec, and then plotting them vertically with an offset. The 0th turn represents the initial lap before the beam interacts with the same lattice elements again. The head and tail spikes in fig. 4.10 is a result of noise in the electronic pulse sent to the UMER gun. The gun is similar to a triode vacuum tube or a MOSFET and can be biased to operate in the saturation regime or the linear amplification regime. Any noise in the pulse delivered between the grid-cathode would not be amplified as much as if it were biased to operate in the linear amplification regime. Since the gun is normally biased to operate in the saturation regime, the spikes are not severe.
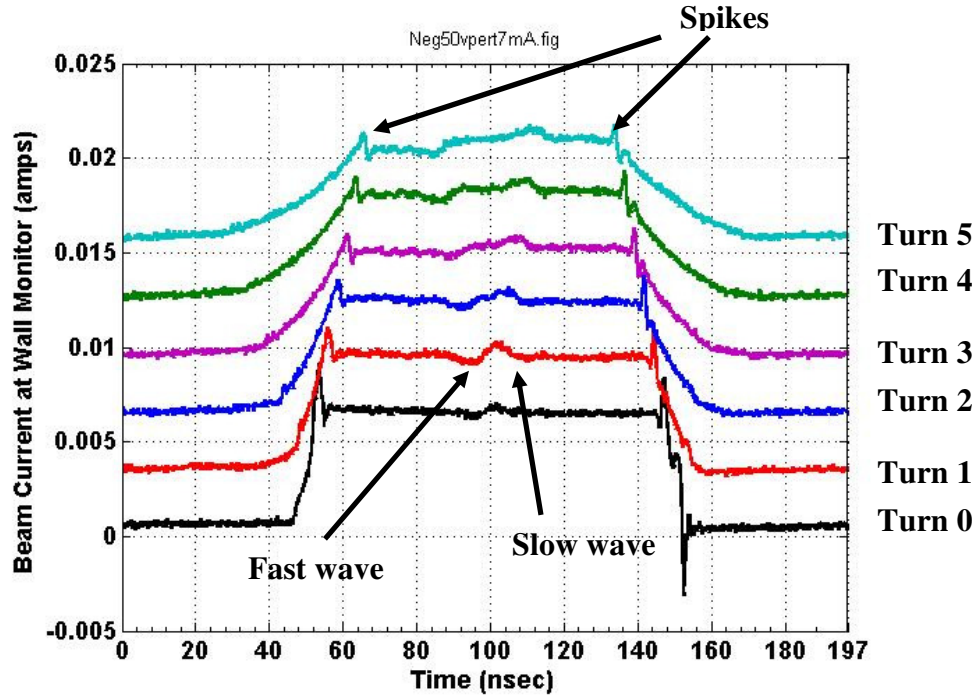
Fig. 4.10 Total current measurement at RC10 for the 7 mA beam and *negative* 50 V perturbation

The δ for this perturbation is $\delta = 0.0707$.

Table 4.4 Measured versus theoretical C_S values for an injected 7 mA beam and *negative* 50 V perturbation

Turn	Experimental- C_S (m/s)	Theoretical- C_S (m/s)	Beam Current (mA)
0	2.60E6 (+/-34.5%)	7.67E5	6.13
1	9.00E5 (+/-25.1%)	7.66E5	6.10
2	8.83E5 (+/-14.4%)	7.52E5	5.85
3	8.47E5 (+/-10.8%)	7.20E5	5.31
4	8.24E5 (+/-8.5%)	7.10E5	5.15
5	8.04E5 (+/-7.2%)	6.85E5	4.76

In this and the following experiments, the waves do not clearly separate during the 0th and 1st turn. This can be seen in fig. 4.10 by the increase in the wave amplitudes from turn 0 to turn 1 as was explained in section 4.2.1. During this particular experiment, there was a 22.3% loss in beam current by the 5th turn which changed the theoretical value of the sound speed by 11%. If we compare the experimental data to the theory, starting from turn 2 to turn 5 and excluding turn 0

and turn 1, there is at most a 15% disagreement with the theoretical calculations. The percent error involved in the experimental measurement is in the placement of the cursor on the curve to determine the Δt. This is displayed in table 4.4 as the percentage of the experimental sound speed.

This same experiment was repeated again but the perturbations level was increased to -100 V.
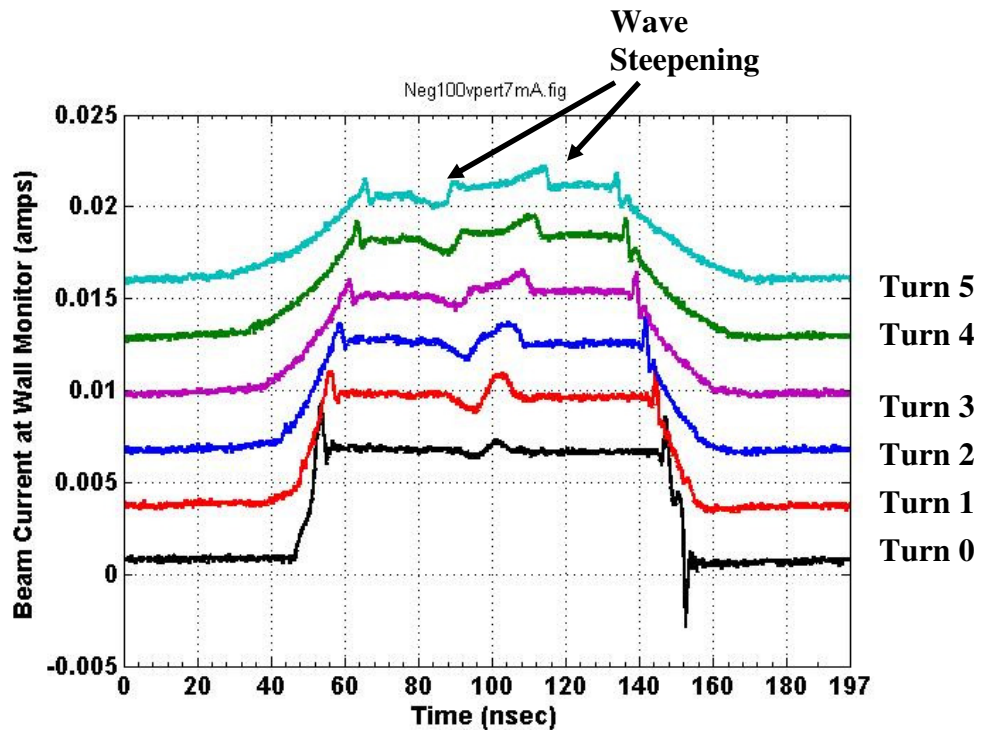
Fig. 4.11 Total current measurement at RC10 for the 7 mA beam and *negative* 100 V perturbation

With the increased perturbation level, where δ for this particular perturbation was $\delta = 0.1$, the measured wave speeds are still within 9.3% of the theoretical values, excluding the initial 0th and 1st measured value because of wave separation. Increasing the level of the perturbation also helps to reduce the error within the measurement, by making the perturbation more noticeable. In figure 4.11, there is

evidence of wave steepening, [refer to section 4.2.3 for wave steepening]. This sharpens the point of the parabolic pulse which helps to reduce the uncertainty in where the cursor should be placed to measure the Δt. The agreement between the experiment and theory for turns 2-4, is within 5.2%. The difference between the experimental measurement and theory, from turns 2-4 and turn 5 is due to another 11% loss in beam current between turns 4 to 5. This would have affected the beam size and as a result, the g-factor. Table 4.6 displays the measured and theoretical sound speeds for this experiment.

Table 4.5 Measured versus theoretical C_S values for an injected 7 mA beam and *negative* 100 V perturbation

Turn	Experimental-C_S (m/s)	Theoretical-C_S (m/s)	Beam Current (mA)
0	2.66E6 (+/-34.4%)	7.62E5	6.03
1	8.45E5 (+/-27.6%)	7.60E5	6.00
2	7.85E5 (+/-16.7%)	7.51E5	5.84
3	7.83E5 (+/-5.9%)	7.42E5	5.68
4	7.78E5 (+/-4.5%)	7.39E5	5.63
5	7.73E5 (+/-3.6%)	7.01E5	5.01

This same experiment and calculations were performed again on the same 7 mA beam current but the polarity of the perturbation was reversed.
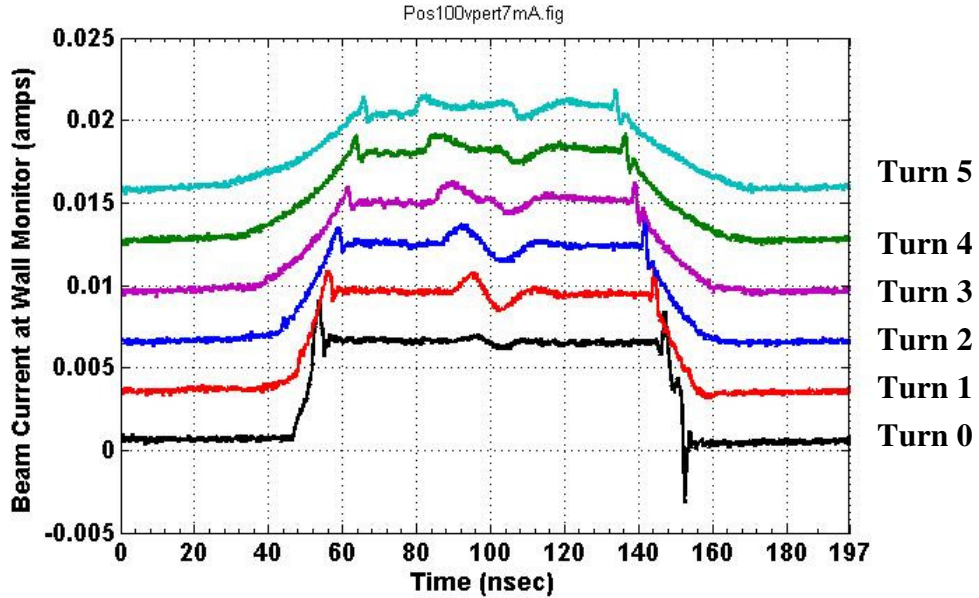
Fig. 4.12 Total current measurement at RC10 for the 7 mA beam
and *positive* 100 V perturbation

In this case, the waves separate and travel along the beam as before but the wave

steepening is in the opposite direction, [refer to section 4.2.3 for wave steepening],

where δ for this particular perturbation was $\delta = 0.1$. The experimentally measured

sound speed agrees with the theoretical value to within 4.8%; excluding the 0th and 1st

turn in both cases.

Table 4.6 Measured versus theoretical C_S values for an injected 7 mA
beam and *positive* 100 V perturbation

Turn	Experimental-C_S (m/s)	Theoretical-C_S (m/s)	Beam Current (mA)
0	2.78E6 (+/-33.0%)	7.67E5	6.13
1	8.47E5 (+/-27.2%)	7.57E5	5.94
2	7.65E5 (+/-17.2%)	7.54E5	5.90
3	7.65E5 (+/-6.0%)	7.33E5	5.54
4	7.54E5 (+/-4.8%)	7.24E5	5.38
5	7.41E5 (+/-3.8%)	7.05E5	5.07

There is still a dramatic loss in beam current, but this time with a positive

perturbation, the loss spreads out over turns 3 to 5. This is probably due to the same

loss mechanism as in section 4.2.1. The fast wave continues to scrap against the beam

pipe as it propagates in the lattice. This results in a gradual loss of charge in the beam

as the perturbation and beam propagates.

4.2.3   Wave Steepening

The steepening of the waves appeared in fig. 4.11 and 4.12 for the

experiments with perturbation strengths of 100 V. The direction in which both the fast

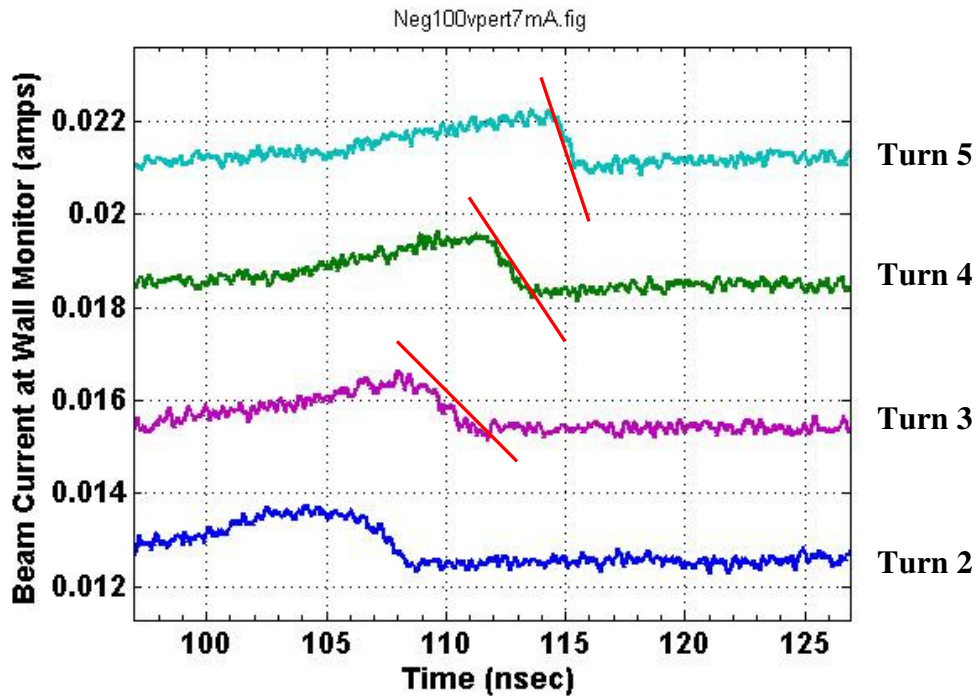and slow waves steepened was dependent on the initial perturbation polarity.

Fig. 4.13 Wave steepening in the slow wave

Figure 4.13 is an expanded view of the slow wave in fig. 4.11. The slope continues to

decrease from -4.3E-4 A/nsec for turn 3 to -1.16E-3 A/nsec for turn 5. The fast wave

also displays the same wave steepening effect but with opposite polarity.

If we observe the wave separation in fig. 4.11, each wave has a negative

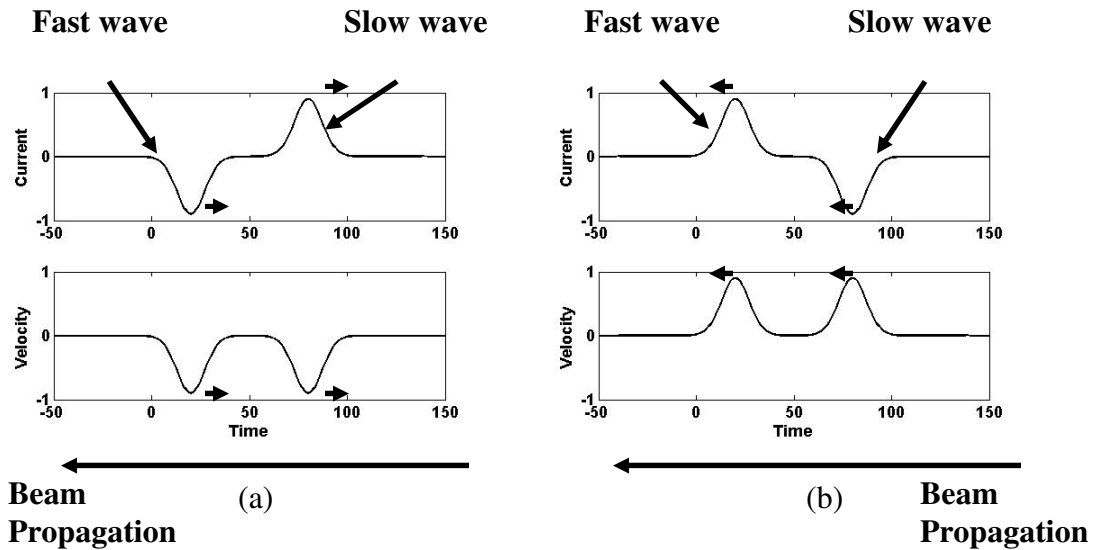velocity profile associated with it as depicted in figure 4.14a.

Fig. 4.14 *Negative* and *positive* wave's scenario

When we have wave steepening for the negative wave scenario, the electrons at the bottom of both waves have a lower velocity magnitude with respect to the main beam. So each wave trough will lag the main beam and steepen to the right. For the positive wave scenario, we have just the opposite case. Each peak has a larger velocity magnitude with respect to the main beam, so each wave peak will get ahead of the main beam and steepen towards the left.

Chapter 5: Conclusion

The purpose of this thesis was to design, simulate and test a device to place longitudinal electric fields as energy (velocity) perturbations on the beam, as well as use a modified version of the device to measure the beam current.

The one-dimensional cold fluid model was reviewed briefly, extracting out that space-charge waves with pure initial velocity perturbations can result in waves both in line-charge density space as well as velocity space that are completely opposite from the case of pure current perturbations.

After that, the induction cell was designed and simulated with Pspice. Since the BEHLKE switch specifications from the manufacture were not representative of the actual circuit, through trial and error, other specifications were found that matched bench tests. Then the induction cell was attached to the pulser with RG-58 and finally bench tested and compared to PSpice simulation results of the same experiment. The ear-fields or gaussians with FWHMs of 8.8 nsec are well within the limitations of the ferrite cores in terms of ferrite saturation. The focal length of the induction cell was explored and compared with the shorter focal length UMER quadrupoles in order to a get a relative idea of the amount of focusing that an induction cell is capable of during normal operating potentials. Comparatively, the induction cell is a weak focusing element.

Finally we used the cell to place velocity perturbations, so to study space-charge waves at short distance from BPM to BPM for half the ring, comparing that to 1-D fluid simulations, getting fairly good agreement with a negative polarity

perturbation. With the opposite perturbation polarity, we get good agreement with the slow wave, but the fast wave appears to loose charge, which is most likely due to scraping against the beam pipe. Long distance studies were also explored, measuring sound speeds for the 7 mA beam over long distances. In some of the data, we obtain 4.8% disagreement between theoretical and experimental sound speed measurements.

Other topics for research:

The first topic that should be further investigated is the perturbations themselves through time-sliced imaging. We can acquire knowledge of beam size and density within the waves over the first turn to help in reducing the discrepancies in sound speed from theory to experiment. When an energy analyzer is installed in the ring, we can perform 1st turn measurements of the waves in velocity space to confirm 1-D theory.

The Dispersion function associated with the lattice elements can effect the perturbation and its resulting waves since they have an energy spread associated with them. By including dispersion into the transfer matrices, we could use space-charge waves as a probe.

These experiments should be simulated in WARP to study the wave steepening and its dependence on the amplitude of the velocity functions in velocity space.

References

[1] R. F. Welton, M.P. Stockli, S.N. Murray, T.A. Justice, Proceedings of EPAC 2004, p. 1538, 2004.

[2] A. Friedman, J.J. Barnard, R.J. Briggs, D.A. Callahan, G.J Caporaso, C.M. Celata, *et al*, "Highly Compressed Ion Beams for High Energy Density Science."

[3] P. G. O'Shea and H. Freund, *Science* 292, p.1853, 2001.

[4] K. Tian, Y. Zou, Y. Cui, I. Haber, R. A. Kishek, M. Reiser and P. G. O'Shea, *PRSTAB*, Vol. **9**, 014201, 2006.

[5] M. Reiser, Theory and Design of Charged Particle Beams, (New York, John Wiley & Sons Inc, 1994).

[6] D. Dowell and P. G. O'Shea, IEEE 0-7803-4376-X, p.1891, 1998.

[7] G. Stupakov and S. Heifets, PRSTAB, Vol. **5**, 054402, 2002.

[8] S. Ramo, *Physical Review*, Vol. **56**, p.276, 1939.

[9] W. C. Hahn, *Gen. Elec. Rev.*, **42**, 258, 1939.

[10] C. Birdsall and J. Whinnery, *J. of Applied Physics*, Vol. **24**, 3, p.314, 1953.

[11] J. G. Wang, D. X. Wang, M. Reiser, *PRL*, Vol. **71**, 12, p.1836, 1993.

[12] H. Suk, J.G. Wang, M. Reiser, Y. Zou, *J. of Applied Physics*, Vol. **86**, 3, p.1699, 1999.

[13] Y. Cui, Ph.D. Dissertation, University of Maryland, 2004.

[14] Y. Huo, Master Thesis, University of Maryland, 2004.

[15] J. Harris, Ph.D. Dissertation, University of Maryland, 2005.

[16] J. C. T. Thangaraj, D.W. Feldman, R.A. Kishek, S. Bernal, *et al*, PAC Proceedings 2007, IEEE Cat. No. 07CH37866, p.3570, 2007.

[17] D. Feldman, A. Valfells, J. Neumann, J. Harris, *et al*, PAC Proceedings 2001, IEEE 0-7803-7191-7, p.2132, 2001.

[18] Behlke Website http://www.behlke.de/

[19] Cheng. D. K., <u>Field and Wave Electromagnetics</u> (2nd Edition), Addison-Wesley Publishing Company, 1989.

[20] BELDEN Website http://www.belden.com/

[21] Ceramic Magnetics, Inc. Website http://www.cmi-ferrite.com/

[22] W. Waldron, private communication, 2007.

[23] M. Dorf, I. Kaganovich, E. Startsev, R. Davidson, E. Lee, presentation slides for NDCX-I HIFS-VNL meeting, 2007.

[24] A. B. EL-Kareh, J. C. J. EL-Kareh, *Electron Beams, Lenses, and Optics I*, Academic Press, 1970.

[25] V. K. Zworykin, G. A. Morton, E. G. Ramberg, J. Hillier, A. W. Vance, *Electron Optics and the Electron Microscope*, John Wiley & Sons, Inc., 1945.

[26] UMER Website http://www.umer.umd.edu/

[27] B. Quinn, B. Beaudoin, S. Bernal, A. Diep, J. Harris, M. Holloway, D. Lamb, *et al*, PAC Proceedings 2003, IEEE 0-7803-7739-9, p.2571, 2003.

[28] FM Technologies UMER Electron Gun Manual.

[29] Bergoz Instrumentation Website http://www.bergoz.com/

[30] D. Stratakis, Ph.D. Dissertation, University of Maryland, 2008.

[31] Y. Zou, Doctoral Dissertation, University of Maryland, 2001.

[32] R. C. Webber, **AIP 212**, Brookhaven, p.85-126, 1990.

[33] K. Tian, Ph.D. Dissertation, University of Maryland, 2008.